



HAL
open science

Locations and Morphologies of Jellyfish Galaxies in A2744 and A370

Callum Bellhouse, Bianca Poggianti, Alessia Moretti, Benedetta Vulcani, Ariel Werle, Marco Gullieuszik, Mario Radovich, Yara Jaffé, Jacopo Fritz, Alessandro Ignesti, et al.

► **To cite this version:**

Callum Bellhouse, Bianca Poggianti, Alessia Moretti, Benedetta Vulcani, Ariel Werle, et al.. Locations and Morphologies of Jellyfish Galaxies in A2744 and A370. *The Astrophysical Journal*, 2022, 937, 10.3847/1538-4357/ac8b6e . insu-03854059

HAL Id: insu-03854059

<https://insu.hal.science/insu-03854059v1>

Submitted on 16 Nov 2022

HAL is a multi-disciplinary open access archive for the deposit and dissemination of scientific research documents, whether they are published or not. The documents may come from teaching and research institutions in France or abroad, or from public or private research centers.

L'archive ouverte pluridisciplinaire **HAL**, est destinée au dépôt et à la diffusion de documents scientifiques de niveau recherche, publiés ou non, émanant des établissements d'enseignement et de recherche français ou étrangers, des laboratoires publics ou privés.



Distributed under a Creative Commons Attribution 4.0 International License



Locations and Morphologies of Jellyfish Galaxies in A2744 and A370

Callum Bellhouse¹, Bianca Poggianti¹, Alessia Moretti¹, Benedetta Vulcani¹, Ariel Werle¹, Marco Gullieuszik¹, Mario Radovich¹, Yara Jaffé², Jacopo Fritz³, Alessandro Ignesti¹, Cecilia Bacchini¹, Neven Tomičić¹, Johan Richard⁴, and Geneviève Soucail⁵

¹ INAF-Padova Astronomical Observatory, Vicolo dell'Osservatorio 5, I-35122 Padova, Italy; callum.bellhouse@inaf.it

² Instituto de Física y Astronomía, Universidad de Valparaíso, Avda. Gran Bretaña 1111 Valparaíso, Chile

³ Instituto de Radioastronomía y Astrofísica, UNAM, Campus Morelia, AP 3-72, CP 58089, Mexico

⁴ Univ Lyon, Univ Lyon1, Ens de Lyon, CNRS, Centre de Recherche Astrophysique de Lyon UMR5574, F-69230, Saint-Genis-Laval, France

⁵ Institut de Recherche en Astrophysique et Planétologie (IRAP), Université de Toulouse, CNRS, UPS, CNES, 14 Av. Edouard Belin, F-31400 Toulouse, France

Received 2022 May 27; revised 2022 August 18; accepted 2022 August 20; published 2022 September 19

Abstract

We present a study of the orbits, environments, and morphologies of 13 ram-pressure stripped galaxies in the massive, intermediate redshift ($z \sim 0.3\text{--}0.4$) galaxy clusters A2744 and A370, using MUSE integral-field spectroscopy and Hubble Space Telescope imaging from the Frontier Fields Program. We compare different measures of the locations and morphologies of the stripped sample with a sample of six post-starburst galaxies identified within the same clusters, as well as the general cluster population. We calculate the phase-space locations of all cluster galaxies and carry out a substructure analysis, finding that the ram-pressure stripped galaxies in A370 are not associated with any substructures, but are likely isolated infalling galaxies. In contrast, the ram-pressure stripped galaxies in A2744 are strictly located within a high-velocity substructure, moving through a region of dense X-ray emitting gas. We conclude that their ram-pressure interactions are likely to be the direct result of the merger between two components of the cluster. Finally, we study the morphologies of the stripped and post-starburst galaxies, using numerical measures to quantify the level of visual disturbances. We explore any morphological deviations of these galaxies from the cluster population, particularly the weaker cases that have been confirmed via the presence of ionized gas tails to be undergoing ram-pressure stripping, but are not strongly visually disturbed in the broadband data. We find that the stripped sample galaxies are generally divergent from the general cluster sample, with post-starburst galaxies being intermediary in morphology between stripped galaxies and red passive cluster members.

Unified Astronomy Thesaurus concepts: [Galaxy clusters \(584\)](#); [Intracluster medium \(858\)](#); [Galaxy interactions \(600\)](#); [Galaxy environments \(2029\)](#); [Galaxy encounters \(592\)](#); [Galaxy evolution \(594\)](#); [Post-starburst galaxies \(2176\)](#)

1. Introduction

The study of galaxy interactions within clusters is critical to understanding the growth and development of galaxies. Many different processes can affect or disrupt a galaxy's gas content, which can have profound effects on its subsequent evolution.

Since the early work of Butcher & Oemler Jr. (1978a, 1978b), it has been understood that the color distribution of a galaxy population evolves with redshift, with greater fractions of blue galaxies at higher redshifts in comparison to the local universe. Many works since then have proposed different mechanisms, both internal to a galaxy, or resulting from interactions with its environment, that can act to transform galaxies and may contribute to the quenching of the global population of galaxies throughout cosmic time.

The environmental processes that act upon cluster galaxies can be divided into gravitational and hydrodynamic effects. The former include *tidal interactions* (Spitzer & Baade 1951; Toomre 1977; Tinsley & Larson 1979; Merritt 1983; Mihos & Hernquist 1994; Springel 2000), caused by direct gravitational interaction between galaxies, and *harassment* (Moore et al. 1996, 1998), resulting from the cumulative effect of many

high-speed close approach encounters between cluster members. In both gravitational processes, the stellar *and* gas components of the galaxies are affected.

On the other hand, lie the processes known as hydrodynamical interactions, which primarily impact the gas component with little to no impact on the prior stellar population. Such effects include the removal of the outer gas reservoir of the affected galaxy via *starvation/strangulation* (Larson et al. 1980; Balogh et al. 2000), and in more extreme cases, the stripping of the internal gas component from the galaxy in the process known as *ram-pressure stripping* (RPS).

First discussed in Gunn & Gott (1972), RPS is one of the most efficient mechanisms (Boselli & Gavazzi 2006) that can abruptly quench star formation and greatly disrupt a galaxy's gas content. RPS can occur when a galaxy moves sufficiently quickly through the dense intracluster medium (ICM) of galaxy clusters. The ram-pressure effect scales with environmental density and galaxy velocity, preferentially affecting galaxies on steep, radially infalling orbits (Jaffé et al. 2018). A galaxy's ability to retain its gas is dependent on its stellar and gas mass surface densities as well as the mass of its dark matter halo, with more massive galaxies able to weather the effect and retain some gas for longer than their less massive counterparts. The ram pressure acts upon the gas component of a galaxy with only a subtle, indirect influence on the existing stellar component (Smith et al. 2012). Observational effects can

include the formation of tails of stripped gas trailing behind the galaxy (Fumagalli et al. 2014), compression of the leading edge of the disk by the ICM (Vollmer et al. 2001), and the onset of star formation in the tails with the condensation of star-forming clumps (Kenney et al. 2014). In addition, it has recently been shown (Bellhouse et al. 2021) that unwinding of the galaxy’s spiral arms can occur during the early stages of RPS, due to removal of material from the outside edges of the disk.

Processes that induce abrupt quenching in cluster galaxies give rise to the population of so-called post-starburst (PSB) galaxies. PSB galaxies exhibit low to negligible star formation characterized by a lack of nebular emission lines, while exhibiting strong Balmer absorption lines indicative of relevant star formation in the past ~ 1 Gyr. Previous studies have pointed toward RPS being responsible, at least in part, for the formation of PSB galaxies in clusters. Evidence includes the correlation of their locations with substructures in the ICM (Poggianti et al. 2004), the similarity in the spectral features of recently quenched regions within RPS galaxies compared with PSB galaxies (Gullieuszik et al. 2017; Werle et al. 2022), and evidence of very recent stripping in certain PSB galaxies (Werle et al. 2022).

Although RPS is known to be one of the most efficient mechanisms influencing the evolution of cluster populations, its relative contribution within the context of galaxy evolution in the universe is only recently starting to be quantified (Vulcani et al. 2022). Many examples of RPS galaxies have been presented to date, including in large surveys of visually selected RPS candidates such as those of Poggianti et al. (2016) and Roberts & Parker (2020) at low redshifts, McPartland et al. (2016) from $0.3 < z < 0.7$, and as part of wider surveys such as the Grism Lens-Amplified Survey from Space (GLASS; Treu et al. 2015; Vulcani et al. 2016, 2017). This has given us an overview of the stripping processes throughout the recent history of the universe and beyond, and newer studies have continued to probe outside the local universe (Boselli et al. 2019; Kalita & Ebeling 2019; Stroe et al. 2020; Durret et al. 2021; Ebeling et al. 2014). Extending the known sample to higher redshifts opens up the opportunity to better understand the impact of stripping on the evolution of clusters, and offers insight into the influence of stripping throughout the history of clusters in the universe today.

A powerful tool in diagnosing and understanding the processes which occur within and around a galaxy is integral field unit (IFU) spectroscopy, which enables the exploration of both the spatial and spectral information of the observed objects. This allows properties such as star formation rates and star formation histories to be traced across a galaxy, and ionized gas to be mapped in location and velocity throughout the galaxy and its tails, making it an extremely useful instrument when characterizing RPS interactions. IFU observations have proven extremely useful in studies of RPS (Merluzzi et al. 2013; Fumagalli et al. 2014; Fossati et al. 2016; Poggianti et al. 2017a), probing the kinematics and ongoing processes within galaxies during infall and leading to new discoveries about the resulting effects of ram-pressure interactions on galaxies (Poggianti et al. 2017b; Bellhouse et al. 2021). In this analysis, we utilize observations gathered by the MUSE (Multi Unit Spectroscopic Explorer, Bacon et al. 2010) IFU at the European Southern Observatory Very Large Telescope.

In this work, we focus on two clusters, A2744 and A370, located around $0.3 < z < 0.4$, which are both post-mergers, and

which are the first two clusters to have been observed within the MUSE Guaranteed Time Observations program.

The aim of this study is to investigate the distribution of identified RPS galaxies in A2744 and A370, both in phase space and within the context of the cluster substructures. We also aim to compare different morphological parameters to test whether these confirmed RPS galaxies could be detectable using automated methods, which could be applied to other frontier fields clusters in a future study.

This paper is part of a series of works that aim to characterize the process of stripping within frontier fields clusters, including Moretti et al. (2022) and Werle et al. (2022).

This paper is structured as follows. Section 2 describes the data used in this analysis as well as the sample selection process. In Section 3, we outline the phase-space and substructure detection techniques used to analyze the distributions of galaxies in the clusters. In Section 4, we compare the locations of the RPS and PSB galaxies with X-ray and mass maps of the clusters. Section 5 describes an analysis of the galaxy morphologies, comparing the RPS and PSB galaxies with the sample of red and blue cluster galaxies, using an array of different morphology measures. Finally, in Section 6 we summarize and interpret the results of the work.

2. Observations and Data

2.1. Clusters

A2744 ($z = 0.3064$, $\sigma = 1497 \text{ km s}^{-1}$, Owers et al. 2011, hereafter A2744) is a merging cluster with a virial mass of $7.4 \times 10^{15} M_{\odot}$, mostly comprised of two distinct components with $v_{\text{pec}} = -1308 \pm 161 \text{ km s}^{-1}$, $\sigma = 1277 \pm 189 \text{ km s}^{-1}$, and $v_{\text{pec}} = 2644 \pm 72 \text{ km s}^{-1}$, $\sigma = 695 \pm 76 \text{ km s}^{-1}$ (Mahler et al. 2018). A2744 is in a particularly dynamic state due to its merging history, with a significant blue galaxy excess of 2.2 ± 0.3 times that of nearby clusters in the same core regions (Owers et al. 2011). The cluster’s merging history is of particular interest, as it provides valuable insight into the link between cluster mergers and galaxy star formation activity. An increased fraction of starbursting blue galaxies driven by interactions with the disturbed ICM is a good candidate for a contributor to the scatter in the Butcher–Oemler effect (Kauffmann 1995; Miller et al. 2006). The complex merging history of A2744 is explored in detail using the X-ray and optical spectroscopy in Owers et al. (2011), who identify two major substructures, the northern core (NC), and the southern minor remnant core (SMRC) within the cluster, as well as a region labeled the central tidal debris (CTD), which is close in projection to the SMRC but exhibits a velocity close to that of the NC and propose a scenario of a post-core-passage major merger in addition to an interloping minor merger, with the CTD being a region stripped from the NC by the interaction. The locations of each of these regions are shown in Figure 12 in the Appendix, for context.

A370 ($z = 0.375$, $\sigma = 1789 \text{ km s}^{-1}$ Richard et al. 2021, hereafter A370) is a historically significant cluster both within the context of galaxy evolution studies (Butcher & Oemler Jr. 1984; Dressler et al. 1997, 1999), and also for the study of gravitational lensing, as it contains one of the first observations of a giant-arc lens system (Lynds & Petrosian 1986; Soucail 1987; Soucail et al. 1988). The cluster has a total virial mass of $M_{\text{vir}} = 3.3 \times 10^{15} M_{\odot}$ from weak lensing measurements (Umetsu et al. 2011b, 2011a). The cluster exhibits a bimodal

distribution of galaxies consistent with a major merger (Richard et al. 2010) of two progenitor clusters with masses $M_{\text{vir}} = 1.7 \times 10^{15} M_{\odot}$ and $M_{\text{vir}} = 1.6 \times 10^{15} M_{\odot}$ (Molnar et al. 2020). The centers of the X-ray and dark matter in both peaks are fairly close in comparison to similar merging clusters, which suggests that the merger axis is predominantly along the line of sight (LoS; Richard et al. 2010). The northern and southern brightest cluster galaxies (BCGs) are located at $z = 0.3780$ and 0.3733 , respectively (Lagattuta et al. 2019), indicating a separation of 1024 km s^{-1} (Molnar et al. 2020). Unlike A2744, the distribution of velocities of the cluster members do not exhibit a distinctly bimodal distribution, suggesting that the merging clusters may have already experienced a previous passage leading to mixing of the populations (Lagattuta et al. 2019).

2.2. Data

In this study, we utilize data from the MUSE Lensing Cluster GTO program (Bacon et al. 2017; Richard et al. 2021). The observations cover the central regions of clusters with single pointings or mosaics, with effective exposure times from 2 hr up to 15 hr under very good seeing conditions ($\sim 0''.6$). The full set of clusters observed with MUSE, described in Richard et al. (2021), is compiled from the MAssive Clusters Survey (MACS; Ebeling et al. 2001), Frontier Fields (FF; Lotz et al. 2017), GLASS (Treu et al. 2015), and the Cluster Lensing and Supernova survey with Hubble (CLASH; Postman et al. 2012) programs. In the case of A2744, the MUSE data consist of a 2×2 mosaic of GTO observations, with a field of view (FoV) of $\sim 2' \times 2'$ ($2' = 0.27 R_{200}$) centered on R.A. = $0^{\text{h}} 14' 20''.952$ and decl. = $-30^{\circ} 23' 53''.88$ covering the region that includes the southern and central structures but excludes the northern core and interloper. (The MUSE FoV of A2744 is shown overlaid on the Hubble Space Telescope (HST) F606W image in Figure 12 in the Appendix.) For A370, the data consist of a 2×2 mosaic of observations centered on R.A. = $2^{\text{h}} 39' 53''.111''$ decl. = $-1^{\circ} 34' 55''.77$, which is an expansion on the single pointing of the GTO program, extending the coverage to a $\sim 2' \times 2'$ ($2' = 0.24 R_{200}$) region of the cluster (Lagattuta et al. 2019). (The MUSE FoV of A370 is shown overlaid on the HST F606W image in Figure 13 in the Appendix). The complete data analysis of the cluster sample and the redshift catalogs are given in Richard et al. (2021). The HST data are comprised of WFPC2, ACS/WFC, and WFC3-IR images, which cover the MUSE observations, sourced from High-Level Science Product images from the CLASH and FF repositories. In this analysis, we use only the data from HST which overlap the MUSE observations in the case of both clusters. In this particular analysis, we make use of the F435W, F606W, and F814W observations from the FF data, and full details of the observations are given in the FF survey paper (Lotz et al. 2017).

For comparison with the cluster mass distribution, we also make use of the Clusters As Telescopes (CATS; Jullo & Kneib 2009; Richard et al. 2014; Jauzac et al. 2015a, 2015b; Limousin et al. 2016; Lagattuta et al. 2017; Mahler et al. 2018) mass surface density model. This model is produced using the LENSTOOL code, which uses the positions, magnitudes, shapes, multiplicity, and redshifts of lensed objects to derive the mass distribution of the cluster. The overall mass distribution is calculated as a superposition of the smooth, global cluster potential, and smaller individual substructures associated with

bright cluster member galaxies. The full methodology of the technique is presented in Jullo & Kneib (2009).

We also utilize X-ray images based on Chandra data, described in Mantz et al. (2010) (see also von der Linden et al. 2014; Vulcani et al. 2017) in order to compare the cluster gas distribution to the locations of the observed RPS and PSB galaxies. The X-ray images use the 0.7–2.0 keV energy band observations, which is the preferred range for tracing gas mass, as the emissivity in this range is largely insensitive to the gas temperature (Mantz et al. 2010).

2.3. Cluster Membership and Galaxy Colors

In order to have an overview of the cluster population against which we can later compare RPS and PSB galaxies, we identify the sample of cluster galaxies within the observed central region by their velocities, and highlight color–magnitude selected red and blue galaxies in order to contextualize our samples within the different cluster populations.

We first extracted the sample of confirmed cluster members by calculating the peculiar velocity of each galaxy using the Richard et al. (2021) spectroscopic redshifts, and selecting galaxies within a specified threshold of the cluster velocity, which was set at $\pm 3 \times (1+z)\sigma$, where σ denotes the cluster velocity dispersion.

For both A2744 and A370, we subdivided the velocity-cut sample into red and blue galaxies using their distribution in F606W–F814W versus F814W color–magnitude space, shown in Figure 1. For each cluster individually, we employed Gaussian mixture models (GMM) to extract two groupings of objects in the color–magnitude space, which closely corresponded to the red sequence and blue cloud. The Gaussian mixture model yields a probability with which each object belongs to either group. We fitted the red sequence by selecting galaxies with a probability > 0.9 of belonging to the upper group of the color–magnitude space, and fit a linear regression line to this sample, marked by the red dashed line in Figure 1.

We then assigned to the red sample all galaxies above the fitted red sequence line, as well as any galaxies below the line with a > 0.9 probability of belonging to the upper group extracted from GMM. All remaining galaxies in the color–magnitude space were then assigned to the blue sample. We further subdivided the blue galaxies into those with F606W–F814W > 0.6 , marked as blue in the figure, and those with intermediate colors, marked in light blue.

For A2744, we spectroscopically confirm 158 cluster members. Of the 148 of these that have good magnitude measurements in F606W and F814W, 114 galaxies are on the red sequence. For A370, we confirm 248 cluster members, 186 with good magnitude measurements in F606W and F814W, of which 116 are on the red sequence.

In the full sample across both clusters, the faintest red sequence galaxy we detect has an F814W magnitude of 25.4, and the faintest blue galaxy we detect has an F814W magnitude of 28.2. For the rest of the analysis, we applied a magnitude limit of 25.5 to both clusters in both the F814W and F606W filters, which is close to our detection limit for red galaxies, but does not exclude any of our RPS or PSB samples. The magnitude limit is shown by the gray shaded region in both panels of Figure 1.

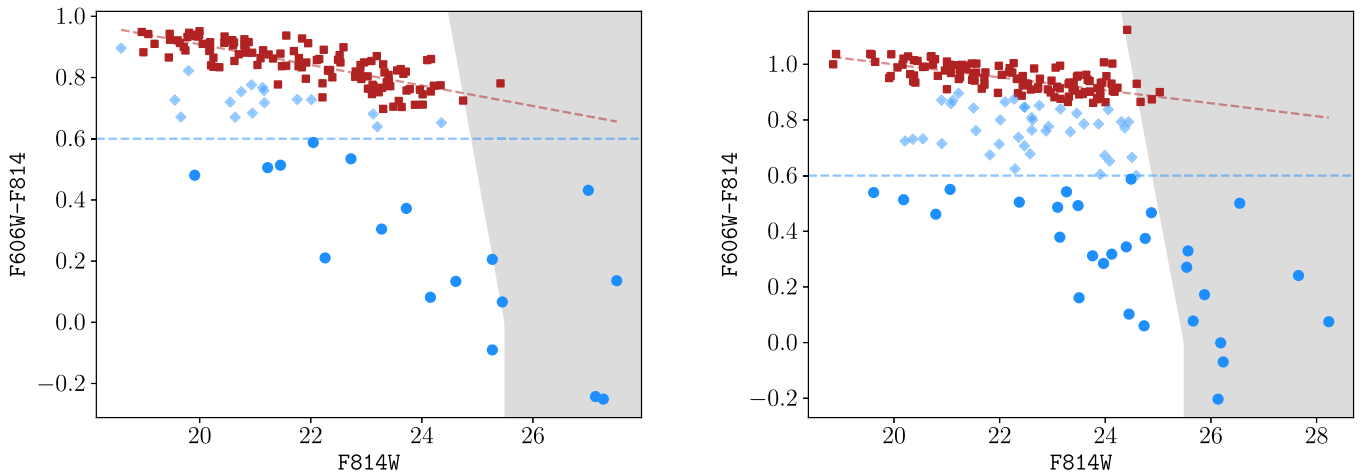


Figure 1. Color–magnitude diagrams for A2744 (*left*) and A370 (*right*), showing all cluster members within the central regions of each cluster covered by the observations. Red galaxies are classified as described in the text (Section 2.3) and marked as red squares. Other galaxies are divided into those with $F606W-F814W > 0.6$, marked as light blue diamonds, and those with $F606W-F814W < 0.6$, marked as blue circles. The red dashed line denotes the linear regression fitted to the red sequence galaxies. The gray shaded region indicates the magnitude limit of 25.5 applied in both the F606W and F814W bands.

2.4. Visual Identification and Sample Selection

We use the samples of galaxies identified in Moretti et al. (2022), who selected RPS and PSB galaxies based on visual inspection of the optical HST data and MUSE spectra simultaneously. Potential RPS galaxies were selected based on the presence of unilateral tails/debris exhibiting emission lines in the MUSE data. Some of the selected galaxies also exhibited tails in the HST data, which were confirmed to be associated with the galaxy from the MUSE redshifts. The PSB galaxies were selected based on their spectral features, targeting objects lacking emission lines associated with ongoing star formation but exhibiting strong Balmer lines in absorption. This classification can be biased against objects that have some ionized gas due to processes other than star formation; however, our spatially resolved data allows us to identify these cases. This is the case of A2744_07, where we find centrally concentrated emission associated with active galactic nuclei (see Werle et al. 2022, for details). The full details of the RPS and PSB sample selection processes are outlined in Moretti et al. (2022). A focused analysis of the PSB galaxies in these clusters, along with others, is presented in Werle et al. (2022).

From Moretti et al. (2022), there are six RPS galaxies as well as four PSB galaxies within the MUSE FoV of A2744. We note, however, two galaxies of interest that show features of being both RPS and PSB (Werle et al. 2022). One of the RPS sample galaxies, A2744_01, has a clear tail in $H\alpha$ but no emission lines within the disk, suggesting that it is in an intermediate phase between the two types. In addition, one of the PSB galaxies, A2744_07, has traces of extraplanar emission, suggestive of a tail from a past stripping event. We primarily classify A2744_01 and A2744_07 as RPS and PSB, respectively, but highlight these galaxies to distinguish them in the rest of the analysis. The locations of the selected galaxies in A2744 are shown marked on the cluster in Figure 12 in the Appendix.

In the case of A370, seven galaxies were visually identified with signs of RPS, along with two PSB galaxies. Two of the galaxies are also noted in other MACS and FF works; A370_01 is highlighted as an extreme case of RPS in Ebeling & Kalita (2019), and A370_08 is noted in Lagattuta et al. (2019) as ID

8006 along with an associated clump of stripped material, ID CL49. The locations of the selected galaxies in A370 are shown marked on the cluster in Figure 13 in the Appendix.

3. Phase-space and Substructure Analysis

In order to explore the cluster environments and to understand the nature of the stripping process for each of the galaxies in our sample, we build a picture of the structure of each cluster and the orbits of the galaxies within using phase-space maps and Dressler–Shectman (Dressler & Shectman 1988, hereafter DS) tests. In general, these diagnostics allow us to better understand how galaxies are interacting with the host cluster, such as the types of orbits they are on and whether they are associated with a group or substructure. Since both clusters are undergoing merging activity, it is particularly important to understand how these galaxies are situated within their environments.

3.1. Phase-space Analysis

The nature of a galaxy’s orbit gives us a useful measure of the likelihood with which it will experience RPS, which is far more common in galaxies passing close to the cluster center at high velocity.

In order to investigate the orbits of the galaxies in our sample, we produced plots of their locations in cluster-projected position–velocity phase space (Hernández-Fernández et al. 2014). These diagnostics reveal the nature of the galaxies’ orbits, allowing us to determine whether they lie on more circular orbits or steep, plunging radial orbits, conducive to RPS (Jaffé et al. 2015). Typically, galaxies at low projected cluster-centric radii with high LoS velocities are likely to be within this regime of orbits (Jaffé et al. 2018), infalling steeply into their host cluster and experiencing RPS.

For the center of A370, we follow the definition given by Lah et al. (2009), who use the midpoint between the northern and southern BCGs. We also use the R_{200} radius of 2.57 Mpc from Lah et al. (2009).

For the center of A2744, we use the coordinates of the BCG closest to the X-ray peak, as used in Owers et al. (2011), and an R_{200} radius of 2.00 Mpc measured by Boschin et al. (2006). For each cluster, we plot the projected radial distance from the

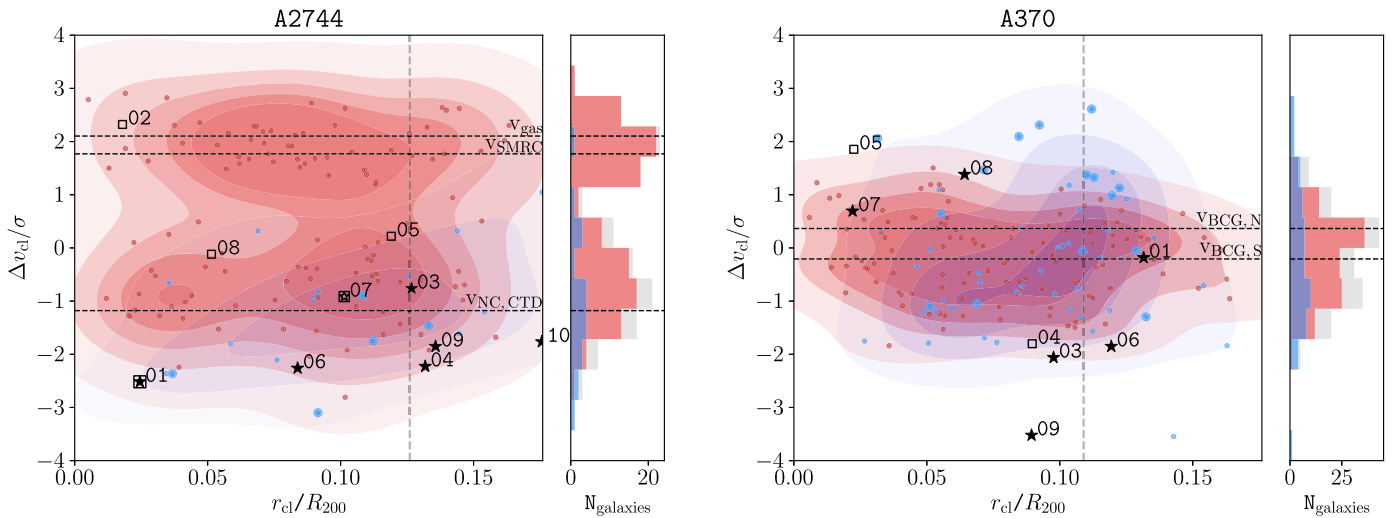


Figure 2. Phase-space diagram for the cluster member galaxies in the MUSE FoV of A2744 (*left*) and A370 (*right*). Galaxies within the color–magnitude red sequence are shown as red points. Galaxies below the red sequence are shown in blue, with galaxies bluer than 0.6 on the color–magnitude diagram highlighted as larger circles. The KDEs of the red and blue galaxy distributions are shown in respectively colored contours. Our sample of RPS galaxies is shown as black stars, while the PSB galaxies are shown as black squares. The vertical gray dashed line denotes the 100% completeness radius described in the text. The vertical histograms show the velocity distributions of each cluster, with the same vertical axis as the phase-space diagrams. The blue and red histograms show the blue and red populations accordingly, with the light gray histogram showing the combined total. *A2744, left:* marked as dashed black lines are the reference velocities of the X-ray gas (v_{gas}), the SMRC (v_{SMRC}), and the velocity of both the NC and CTD ($v_{\text{NC,CTD}}$), from Owers et al. (2011). A2744_01 and A2744_07 are marked as both RPS and PSB, for the reasons described in Section 2.4. The cluster is clearly bimodal in velocity distribution from the histogram, and the majority of blue galaxies and RPS galaxies are located in the blueshifted component. *A370, right:* black dashed lines indicate the reference velocities of the northern and southern BCGs, from (Lagattuta et al. 2019), as explained in the text. From the velocity histogram, the cluster appears to have a comparably singular velocity distribution in contrast to A2744 and the two merging components do not appear to be significantly separated. Furthermore, the blue galaxies are distributed across a wider range of velocities compared with the red galaxies. The RPS galaxies, PSB galaxies, and the majority of the bluest galaxies with $F606W-F814W > 0.6$ are generally situated at extremes in velocity with respect to the observed component of the cluster.

center relative to R_{200} and the LoS velocity deviation from the cluster average, relative to the cluster global velocity dispersion, for all cluster galaxies. The resulting phase-space diagrams are shown in Figure 2. The galaxies are divided into red and blue (and marked with accordingly colored points) based on the red sequence classification described in Section 2.3. Red- and blue-filled contours show the kernel density estimates (KDEs) of their respective galaxy samples, to better visualize their distribution within phase space. We mark the galaxies in our RPS sample with solid black stars, and the PSB galaxies with open black squares. In both figures, we denote a 100% azimuthal completeness radius with a vertical dashed gray line. A circular aperture larger than this radius begins to extend beyond the boundaries of the square FoV of MUSE, therefore limiting the number count of visible galaxies. We also mark the average velocities of three important regions described in Section 2.1, measured by Owers et al. (2011), which are the NC, CTD, and SMRC, as well as the X-ray velocity from the same paper, of the region therein described as MISC2.

The phase-space diagram for A2744 shows the extremely disturbed, non-virialized nature of the cluster. Two distinct clumps are visible with a velocity separation of approximately 3σ . The clump at -1σ contains all galaxies in the RPS sample, as well as a much higher fraction of blue galaxies. The difference in the blue fraction between the two components could be the result of increased star formation (Vulcani et al. 2018) in the CTD galaxies due to mild interaction with the ICM (Stroe et al. 2017, 2020), or a higher quenched fraction in the SMRC as a result of its previous merging history.

In addition to this, some of our RPS galaxies are located within the MISC2 region identified in Owers et al. (2011), corresponding to the X-ray surface-brightness peak, shown in

Figure 12 in the Appendix. In Owers et al. (2011), a value of $0.3189^{+0.0092}_{-0.0110}$ was measured for the redshift of the X-ray emission, yielding a peculiar velocity of $2854.78 \text{ km s}^{-1}$ (marked v_{gas} in the left panel of Figure 2). This velocity is very similar to the velocity of galaxies in the SMRC (marked v_{SMRC} in the same figure), and greatly offset from our sample of RPS and PSB galaxies.

The measured velocities of the RPS sample, as well as the velocities of the merging components of the cluster and the X-ray emitting gas, suggest that the RPS galaxies and most of the PSB galaxies are associated with the NC/CTD, but are passing through a region of gas that is moving with the SMRC. The extreme difference in velocity between the galaxies in this region and the cospatial gas is likely to be inducing the ram-pressure effect observed in our sample of RPS galaxies. This also corroborates the hypothesis put forward by Owers et al. (2011) that the CTD region consists of tidal debris removed from the main cluster (now the NC) during the core-passage phase of its merger with the SMRC.

In the case of A370, the phase-space diagram shows a comparatively more relaxed distribution of galaxies, despite A370 also being a merging cluster. The observed portion of the cluster has a skewed but single-peaked redshift distribution, as seen in the right-hand panel of Figure 2. The velocities of the northern and southern BCGs are indicated as black dashed lines on the figure. Previous studies (Lagattuta et al. 2019; Molnar et al. 2020) have noted that there are no prominent subgroups associated with the velocities of the BCGs. Instead, the velocities of the cluster galaxies appear to follow a more uniform Gaussian distribution.

The blue galaxies in A370 are generally located at higher cluster-centric radii (median cluster-centric distance: 0.25 Mpc , $0.10 R_{200}$) compared with the red galaxies (median cluster-

centric distance: 0.19 Mpc, $0.07 R_{200}$) and the velocity dispersion of the blue galaxies ($\sigma_{\text{blue}} = 2251 \text{ km s}^{-1}$) is higher than that of the red galaxies ($\sigma_{\text{red}} = 1320 \text{ km s}^{-1}$). The velocity distribution of blue galaxies also appears to be slightly skewed toward negative values according to the histogram, although not as prominently as in A2744. Two sample Kolmogorov–Smirnov (K-S) tests reveal that at the 10% significance level, the two populations follow the same velocity distribution ($p = 0.14$) but distinct distributions in cluster-centric radius ($p = 0.05$). The RPS and PSB galaxies in our sample are generally located at high positive and negative LoS velocities and are not restricted to any particular region, but are distributed throughout the cluster. The high LoS velocities of the galaxies are conducive to ram pressure due to the velocity difference between the galaxies and the ICM, while the scatter in locations suggests that infall is the root cause, in contrast to a large-scale movement or cluster interaction, which would affect galaxies in a specific region as we observe in A2744.

We therefore find two different stories regarding the cause of RPS between these two clusters. In the case of A2744, the RPS galaxies are likely to be experiencing an intense interaction with the ICM in the CTD region, directly resulting from the merging activity of the cluster. The galaxies, likely part of the CTD stripped from the NC, are colliding with a dense region of the ICM associated with the SMRC, which has a significantly different velocity. Similar scenarios of merger-induced RPS have previously been discussed in other clusters (Ebeling & Kalita 2019; Stroe et al. 2020). In contrast, within the observed region of A370, the RPS galaxies appear to be isolated infallers, experiencing ram pressure as they accelerate into the cluster potential well. If, as discussed in Lagattuta et al. (2019), the cluster has undergone an initial passage, it is possible that the disturbance of the ICM is enhancing the ram pressure, but we do not observe a consistent, large-scale motion as in A2744.

3.2. Cluster Substructure Analysis

We carry out DS tests (Dressler 1980; Knebe & Müller 2000) to investigate where our galaxy samples are located within the context of the clusters’ substructures. The DS test compares the velocity distribution of each galaxy and its 10 nearest neighbors to the velocity distribution of the cluster to identify regions of consistent velocity that are significantly offset from the cluster in general, indicative of a group or substructure.

For each galaxy and its 10 nearest neighbors, we measure the group standard deviation σ_g using the gapper method (Beers et al. 1990) taking the differences between the sorted velocities of the galaxies and weighting by an approximately Gaussian envelope.

The deviation of each galaxy and its nearby companions is then defined as

$$\delta^2 = \frac{11}{\sigma_{\text{cl}}^2} [(\bar{v}_{g, \text{pec}})^2 + (\sigma_g - \sigma_{\text{cl}})^2],$$

where σ_{cl} is the cluster standard deviation measured from the literature, σ_g is the gapper method standard deviation of the group, and $\bar{v}_{g, \text{pec}}$ is the group mean peculiar velocity, $\bar{v}_{g, \text{pec}} = \bar{v}_g - \bar{v}_{\text{cl}}$.

The value of δ gives a measure of the local deviation in velocity from the cluster as a whole. Groups of galaxies with similar velocities that are significantly different from the cluster

average will have higher deviations, highlighting possible regions that kinematically stand out from the cluster as a whole.

In the case of A2744, Owers et al. (2011) consider the system to be a post-core merger, and due to the recent core passage, the main structures are still not fully disrupted and are clearly separated in velocity (as shown in the left panel of Figure 2). In this work, we focus on the smaller FoV of the MUSE observations, which exclude the NC but cover the SMRC and CTD structures (see Figure 12 in the Appendix). To better separate the SMRC and CTD structures, we perform the DS analysis considering the SMRC as the main structure, which naturally highlights the deviation of galaxies potentially belonging to the CTD (see the left panel of Figure 2). We note, additionally, that we also tried performing the DS test using the average velocity and velocity dispersion of all the cluster galaxies measured by Owers et al. (2011) and found signs of deviation in both groups, confirming this result (not shown).

The DS test results are shown in Figure 3 for both clusters. Galaxies in the clusters are shown as circles, with the size corresponding to their δ value. The size scale is enhanced $10\times$ in the case of A370 for clarity. Close groups of large circles are indicative of regions of substructure, where several galaxies are moving with a significantly deviated velocity from the cluster average. The limiting threshold on the delta value, indicating a significant deviation from the cluster velocity, is calculated to be $3 \times \sigma_\delta$, where σ_δ is the standard deviation of all velocity deviation values in the given cluster (Girardi et al. 1996; Olave-Rojas et al. 2018). Galaxies with a δ above this limit are shown with filled points, while those below the limit are shown unfilled. The RPS galaxies are marked with stars and the PSB galaxies are marked with squares. A2744_01 is marked as both RPS and PSB for the reasons outlined in Section 2.4.

The DS test for A2744 indicates that many galaxies are moving with velocities that are significantly deviated from the SMRC. This is expected, considering the cluster is undergoing a significant merging event, and the majority of galaxies in the FoV are associated with different merging components. Our DS test for this region of the cluster concurs with the results of Owers et al. (2011), the most significant substructure in the FoV is the CTD, visible across the northwest half of the figure as a grouping of large circles. All of the ram-pressure stripped galaxies and PSB galaxies in our sample are parts of some velocity substructure, which is also expected if the merging of the different components is driving the onset of stripping.

Combining these results with the phase-space analysis, we find that several pieces of evidence consolidate the hypothesis that these galaxies are experiencing a magnified interaction with the ICM resulting from the merger event:

1. The presence of many RPS and PSB galaxies in the velocity component at -1σ , along with the difference in the blue galaxy fraction compared with the component at 2σ .
2. The location of these galaxies within or close to the region postulated by Owers et al. (2011) as the CTD (shown by the gray circle in Figure 3 and the green circle in Figure 12 in the Appendix), resulting from the major merger of the clusters.
3. The velocity of these galaxies being similar to the average velocity of galaxies in the CTD and the NC (marked v_{NC} in the left-hand panel of Figure 2, measured by Owers et al. (2011)).

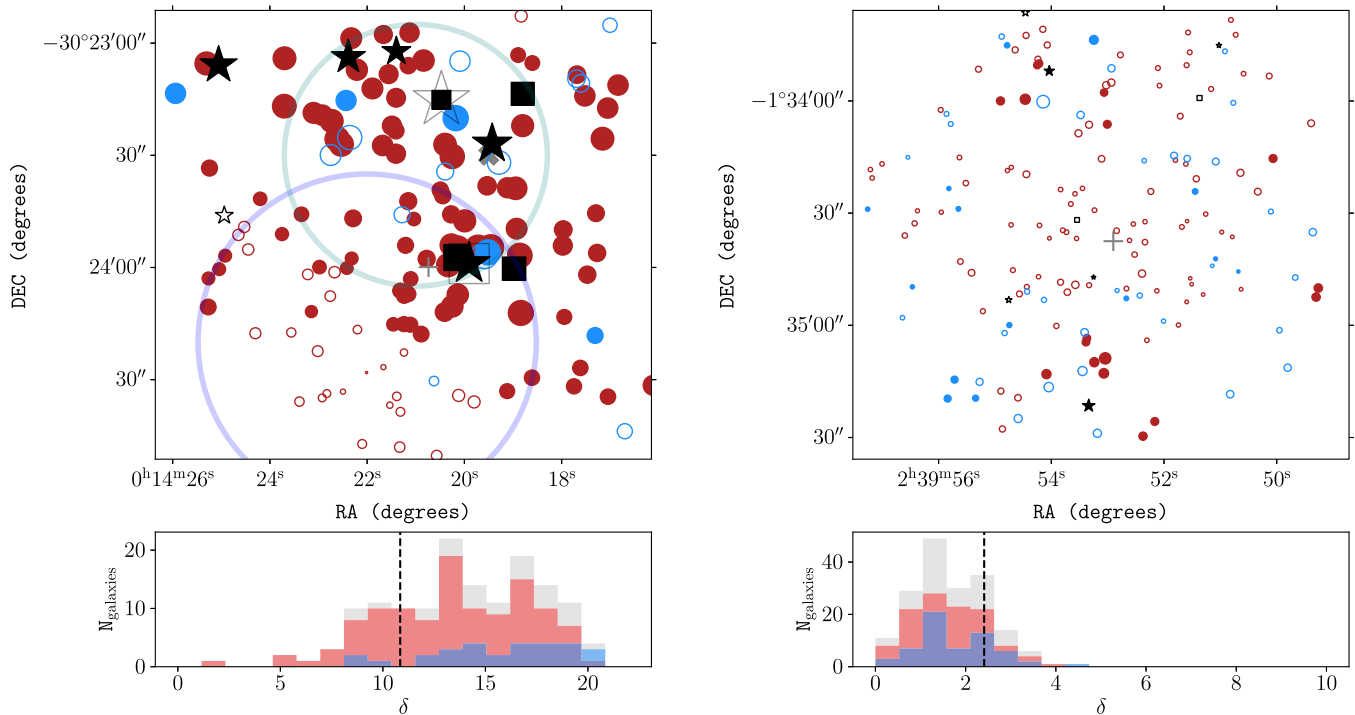


Figure 3. DS tests for A2744 (*left*) and A370 (*right*), showing a bubble plot in the upper panel and a histogram of the delta distribution in the lower panel. Galaxies are shown as circles, highlighted red if they lie on the red sequence described in Section 2.3, or blue otherwise. Black stars indicate the ram-pressure stripped sample and black squares indicate the PSB sample. A2744_01 is highlighted as a black star in a light gray square, while A2744_07 is highlighted as a black square in a light gray star, for the reasons explained in Section 2.4. All points on the figure are filled if their velocity deviation surpasses the substructure threshold described in the text (black dashed line in lower panel), or unfilled otherwise. The cluster centers used in this analysis are marked with + symbols. The histograms below each plot show the distribution of delta values from the DS test for blue and red galaxies, colored accordingly, with the total combining both colors shown in gray. Black dashed vertical lines indicate the threshold for substructure as described in the text. For A2744, we mark on the bubble plot the regions of interest defined in Owers et al. (2011): the light green circle marks the CTD, the blue circle marks the SMRC, and the gray X marks the location of the X-ray surface-brightness peak.

The DS test for A370 highlights a more relaxed distribution of galaxies within the observed region of the cluster in comparison to A2744. The majority of galaxies within the MUSE FoV are not indicated to reside within any separate substructures, and only a few significant substructures are detected, to the northeast, southwest, and to a lesser extent, the west of the figure. All but two of the RPS galaxies and all of the PSB galaxies are not located within any of the detected substructures, which may suggest that the majority of our sample entered the cluster as isolated galaxies.

4. Comparison with X-Ray and Gravitational Lensing Analysis

4.1. X-Ray and Mass Surface Density Maps

In order to investigate the distribution of RPS and PSB galaxies within the environment of the cluster, we plotted the locations of the galaxies overlaid on the X-ray and the lensing modeled mass surface density maps, shown in Figures 4 and 5 for A2744 and A370, respectively. For both clusters, we show the CATS version 4 (Lagattuta et al. 2017, 2019; Mahler et al. 2018) mass surface density map in cyan and the Chandra X-ray image (Mantz et al. 2010; von der Linden et al. 2014; Vulcani et al. 2017) in magenta. For display purposes, the X-ray images were smoothed with a 3×3 median filter and convolved with a 5×5 Gaussian kernel. For each of the RPS and PSB galaxies, we plot the cleaned HST F606W map in white, as well as the MUSE $H\alpha$ map shown in yellow. The $H\alpha$ map was produced using our custom-made emission-line fitting software HIGHSELF (M. Radovich et al. 2022, in preparation), which is based on the

LMFIT python library (<https://lmfit-py.readthedocs.io/>) and fits a user-defined set of emission lines using one or two Gaussian components (see Moretti et al. 2022, Section 3 therein for full details of the measurement). The white x marks in each figure show the centers of the clusters used in this study.

The cluster maps highlight the differences between the observed regions of the clusters. A2744 has a prominently disturbed gas component, shown by the X-ray map, with the majority of the X-ray emitting gas located to the upper right of the observed region. The mass component, shown by the lensing modeled mass surface density map, is distinct from the X-ray component and the majority of the mass is located to the lower left of the X-ray emission. This large difference between the galaxies and gas is attributed in Owers et al. (2011) to the collision between the major components of the cluster, which has decoupled the gas component from the collisionless galaxies and dark matter components.

In comparison, the X-ray and mass surface density maps for A370 are coincident, with the peak of the X-ray emission lying between the two peaks of the mass map (see also Lagattuta et al. 2017, Figure 10).

In the case of A2744, as discussed in Section 3.1, the majority of the PSB and RPS galaxies in our sample are located within the X-ray region, to the upper and/or right of the majority of the mass distribution. This X-ray emitting gas has a high velocity offset from the RPS and PSB galaxies. Since this velocity offset is the result of the merger between this subcluster and the NC, the merging activity appears to be driving the RPS interactions, rather than infall alone. In particular, the RPS is being enhanced by the collision between the galaxies associated with one

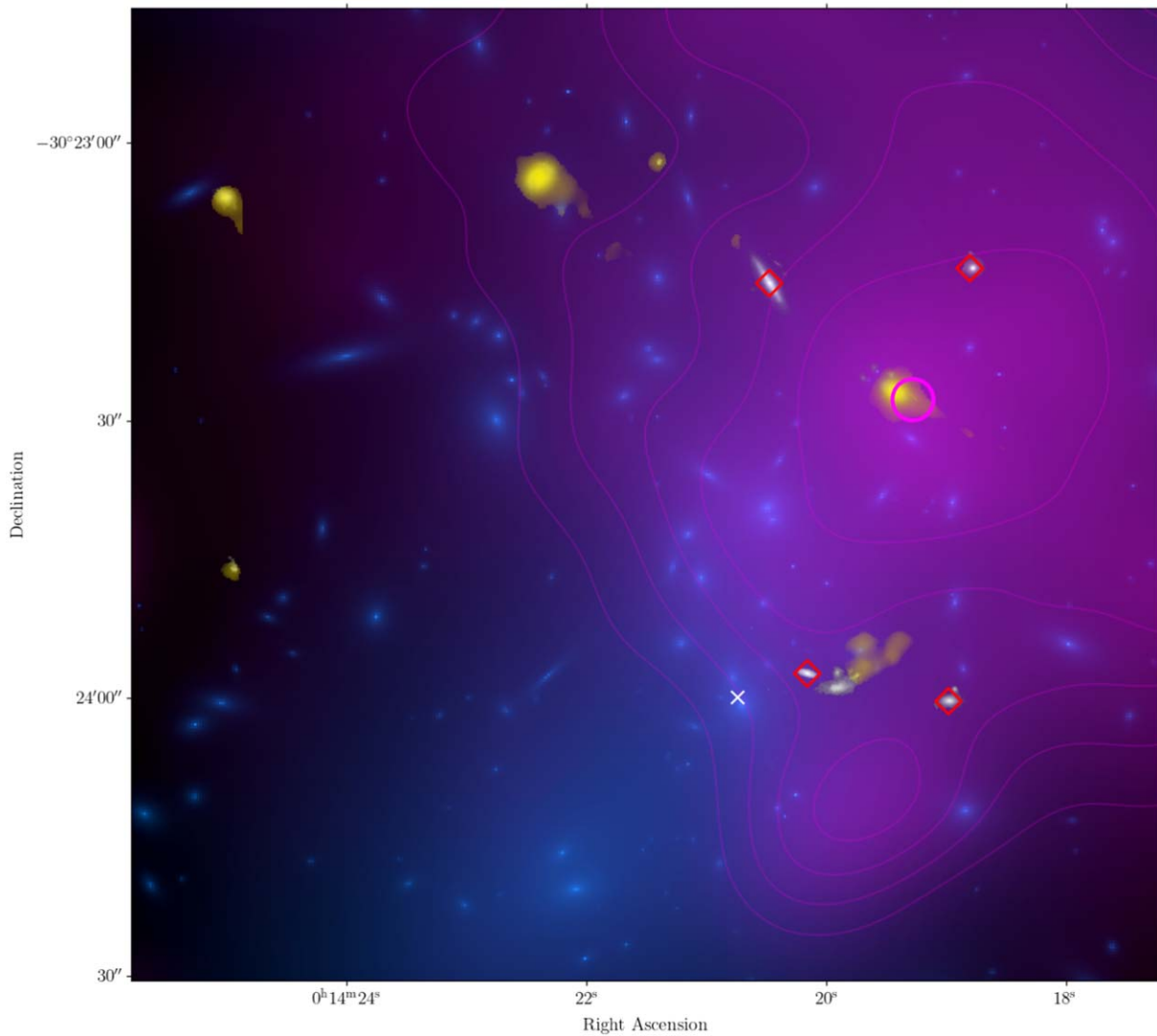


Figure 4. X-ray and lensing maps of A2744 with F606W + $H\alpha$ maps of RPS galaxies and PSBs overlaid. The magenta image and contours show the smoothed X-ray map from Chandra. The CATS v4 lensing mass map is shown in cyan. F606W images of RPS and PSB galaxies are shown in white, with MUSE $H\alpha$ maps shown in yellow. PSB galaxies are marked with red diamonds. The cluster center used in the analysis is marked with a white X. The peak in the X-ray emission is marked with a magenta circle.

merging component, and the gas associated with another merging component. One galaxy of interest in this cluster is A2744_01, which was classified both as an RPS and PSB galaxy, due to its long tail of stripped material but lack of star formation or nebular emission lines. The direction of the galaxy’s tail suggests that it has recently passed through the region characterized by very strong ICM X-ray emission, indicating that the galaxy may have just exited a phase of very strong RPS.

For A370, the RPS and PSB galaxies are more uniformly distributed around the cluster, and not constrained to a particular region. Together with the more uniform distribution of the X-ray component and its alignment with the mass surface density distribution, this suggests that the galaxies are undergoing stripping due to infall rather than collision with a merging component’s ICM as in A2744.

4.2. Comparing ICM X-Ray Emission

Several works have explored the correlation between stripping efficiency and the presence of X-ray gradients and shocks from the ICM (Owers et al. 2012; Vijayaraghavan &

Ricker 2013). Vulcani et al. (2017) observed that in unrelaxed clusters, $H\alpha$ emitter properties exhibit slight trends with the local ICM X-ray emission, suggesting that some form of interaction with these features may be responsible for the stripping of gas and/or triggering of star formation. In addition, Stroe et al. (2020) find strong evidence for triggering of star formation by shocks produced by merging activity in the post-core passage merging cluster CIZA J2242.8+5301, nicknamed the Sausage cluster. The alignment of disturbed features in the Sausage cluster galaxies with the merger axis of the cluster strongly indicates that the galaxies have been disturbed by interactions with the traveling shock fronts in the ICM. In order to investigate whether we see a correlation between stripping activity and ICM X-ray emission, we investigated the coincident X-ray flux of the ICM at the locations of the galaxies in our sample with the cluster members. To do this we calculated the median X-ray flux within an annulus, avoiding any X-ray emission from the galaxies themselves, between 15 and 30 kpc from the location of each galaxy. The X-ray fluxes are shown in Figure 6 for A2744 (*top*) and A370 (*bottom*) with the RPS

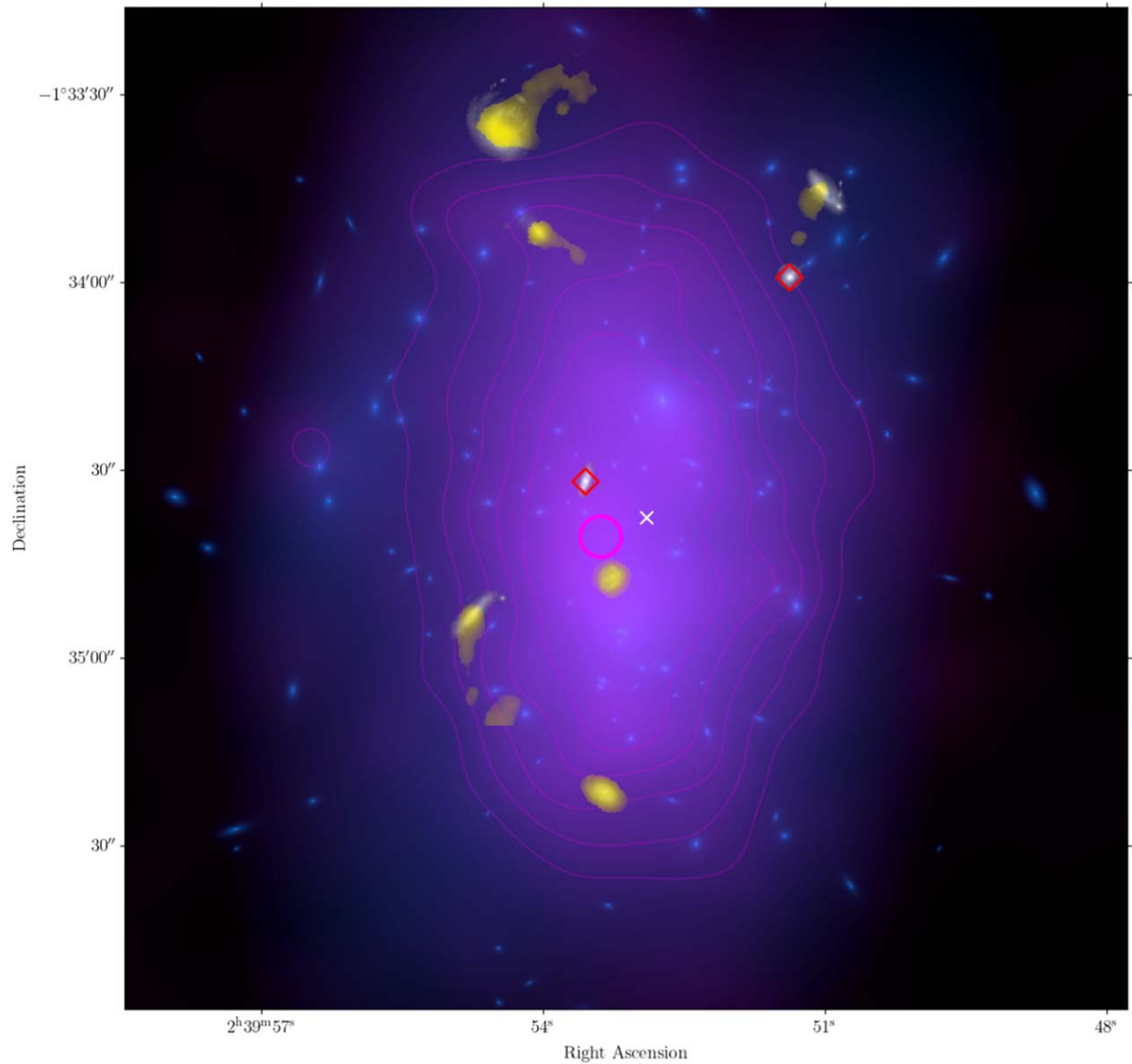


Figure 5. X-ray and lensing maps of A370 with F606W + H α maps of RPS galaxies and PSBs overlaid. The magenta image and contours show the smoothed X-ray map from Chandra. The CATS v4 lensing mass map is shown in cyan. Whitelight images of RPS and PSB galaxies are shown in white, with MUSE H α maps shown in yellow. PSB galaxies are marked with red diamonds. The cluster center used in the analysis is marked with a white X. The peak in the X-ray emission is marked with a magenta circle.

galaxies marked in black and white hatching and PSB galaxies marked in gray. The general population of blue cluster galaxies is shown in blue for comparison. We tentatively observe in both clusters that PSB galaxies are generally found within regions of higher X-ray flux emission from the ICM, in comparison to blue cluster galaxies. In the case of A370, the population of RPS galaxies are also found in regions of higher ICM X-ray emission compared with blue cluster galaxies, while in A2744 the distribution of ICM X-ray emission is comparable to, or lower than that of the blue cluster galaxies. The differences between the samples are small, however. Two sample K-S tests revealed no distinction at the 5% significance level between the distributions of the RPS and PSB galaxies compared with the blue cluster galaxies in both A2744 ($p_{\text{RPS}} = 0.58$, $p_{\text{PSB}} = 0.27$) and A370 ($p_{\text{RPS}} = 0.28$, $p_{\text{PSB}} = 0.71$) individually. On the other hand, when the two clusters are combined as shown in Figure 7, the distribution of PSBs becomes distinct from the blue cluster galaxies ($p_{\text{PSB}} = 0.04$).

In general, A2744 appears to be too disturbed to draw a reliable conclusion on its own. Compared with A370, the distribution of blue galaxies in A2744 appears to be pushed toward higher X-ray fluxes, which may be due to the dearth of blue galaxies in the SMRC (which corresponds a region of generally lower X-ray emission) resulting from its past minor merger.

While we emphasize the caveat that the 3D distribution of the disturbed cluster ICM and the 3D locations of the galaxies are not known, our result for the PSB galaxies may be consistent with the progression of galaxies through the RPS stage as they pass through denser regions of the ICM into the PSB phase. Galaxies encountering interactions with denser regions of the ICM are expected to be subjected to more intense RPS, up to the point that the gas becomes fully stripped and the galaxy becomes a PSB galaxy. In this case, galaxies located in denser regions of the ICM may have already been stripped to the point of becoming PSB.

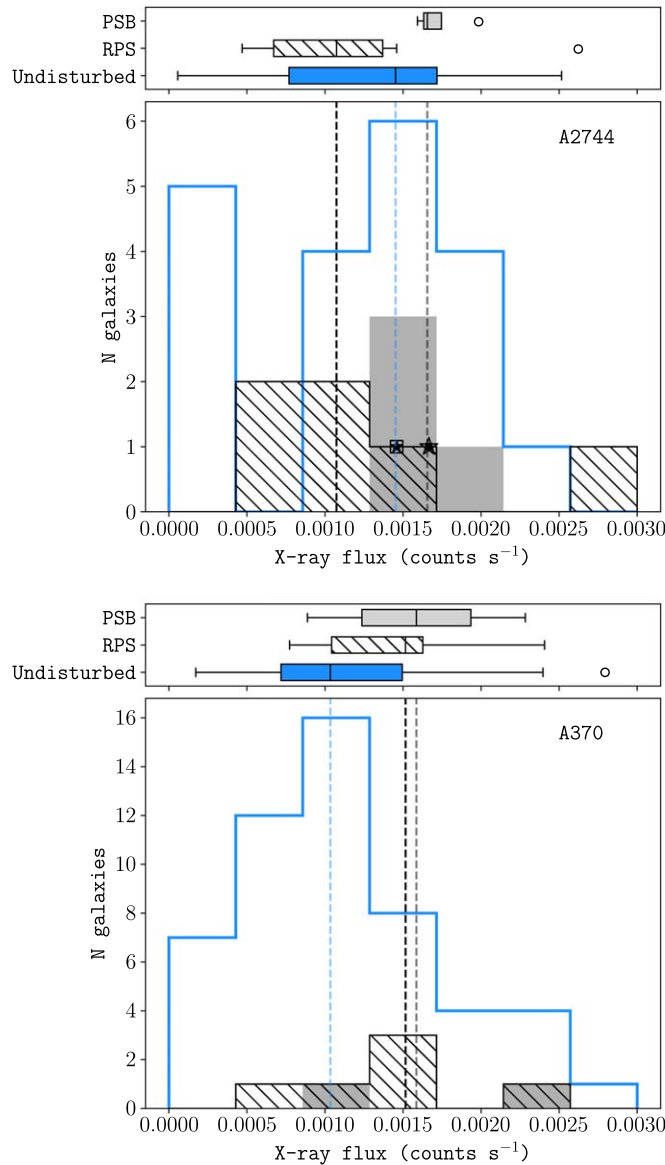


Figure 6. Histogram of coincident ICM X-ray fluxes at the locations of all PSB galaxies (gray shaded) all RPS galaxies (black hashed) and all remaining blue cluster galaxies (blue) for A2744 (*top*) and A370 (*bottom*). The median values for the ICM X-ray flux for each sample are plotted as dashed vertical lines with the same colors. The location of A2744_01 is highlighted with a black star in a hollow box, while the location of A2744_07 is highlighted as a black box in a hollow star, for the reasons explained in Section 2.4.

Our findings for the PSB galaxies may also be consistent with Vulcani et al. (2017), who measured the offset between the peaks of the $H\alpha$ and F475W emission projected along the cluster radial direction, for cluster galaxies in the GLASS survey, and found that a correlation emerged with the ICM X-ray emission for galaxies in unrelaxed clusters.

5. Morphology Analysis

We utilize several quantitative measures of the morphologies to understand whether our RPS and PSB galaxies occupy a specific region of morphology space. The selection of RPS and PSB galaxies, based on the presence of $H\alpha$ tails measured from the MUSE data, allows us to better explore their distribution in terms of visual morphological parameters, since the selection is not strictly biased toward galaxies with notable visual disturbances. Many galaxies in our sample appear fairly undisturbed in

broadband imaging, but have clear tails in the MUSE data. This allows us to test the sensitivity of these parameters in order to determine whether subtle cases of RPS can still be differentiated from the general cluster population using this analysis.

We also investigate whether this analysis is improved by the inclusion of multiple broadband filters, to incorporate color measurements, or if one broadband filter is sufficient. This will determine the minimum requirements for potential sample selections based solely on these techniques.

For each galaxy, we make a cutout from the F606W HST image and use the python package *statmorph* (Rodríguez-Gomez et al. 2019) to extract different morphological parameters. We ran the *statmorph* function *source_morphology* using the segmentation maps produced by the GTO pipeline, with a gain of 2.5 and a point-spread function generated using *sExtractor*. Weight maps and masks were not used in this case. The cutouts, segmentation maps, and

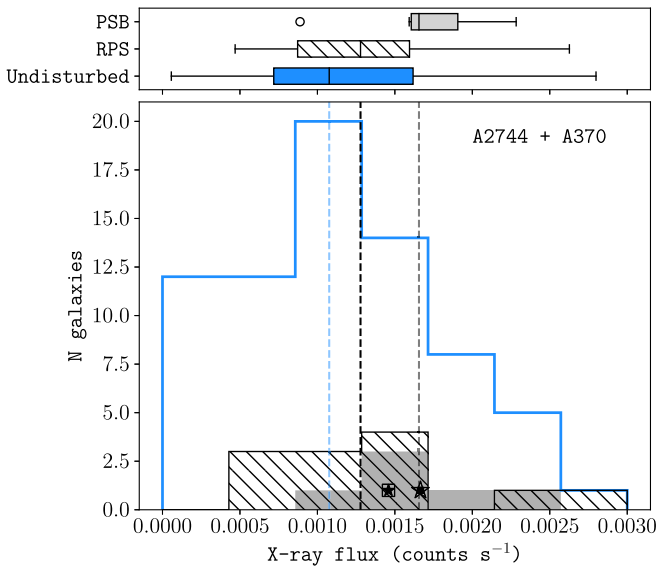


Figure 7. Histogram of coincident ICM X-ray fluxes at the locations of all PSB galaxies (gray shaded) all RPS galaxies (black hashed) and all remaining blue cluster galaxies (blue) for A2744 and A370 combined. The lines and symbols are as described in Figure 6.

resulting morphological parameters are shown for a few examples in Figure 17 in the Appendix.

We focus on the morphological quantities *concentration* and *asymmetry* (Conselice 2003, 2014), as well as Gini (Glasser 1962; Abraham et al. 2003; Lotz et al. 2004) and M_{20} (Lotz et al. 2004). We note here brief summaries of the morphological parameters used and refer the reader to Roberts & Parker (2020) for an effective summary and the original papers cited here for the full details.

The concentration measure (Conselice 2003, 2014) is derived from the ratio of the radii that contain 80% and 20% of the total luminosity of a galaxy, giving an indication of the steepness of the light profile of the source.

The asymmetry (Conselice 2003, 2014) parameter is defined as the difference between the flux map of a galaxy and its 180° rotated counterpart. This parameter is particularly suitable for detecting the asymmetric offsets and disturbances expected during RPS interactions. We note also the *shape asymmetry* (Pawlik et al. 2016) parameter, utilized in Roberts & Parker (2020), which uses the binary detection map instead of the total flux map. This parameter is more sensitive to low surface-brightness features, making it ideal for detecting the disturbances visible in RPS; however, the observations we use in this study have particularly crowded fields, impacting the shape of the detection maps. We found that the standard asymmetry, while less sensitive to low surface-brightness features, was a more robust measure in a crowded environment.

The Gini parameter (Glasser 1962) is traditionally used within the context of economics and parametrizes the distribution of wealth across a population. The parameter has also been utilized in astronomy to quantify the distribution of flux in an image, with lower values indicating a more homogeneous distribution and higher values describing a more concentrated source of flux.

Finally, the M_{20} statistic is the ratio of the second order moment of the brightest 20% of pixels in a galaxy’s image and the second order moment of the entire image. This parameter is

sensitive to bright features offset from the galaxy center, which makes it suitable for detecting large disturbances in a galaxy’s morphology.

We combine the parameters concentration and asymmetry in the top-left panel of Figure 8 for both A2744 and A370 together. In the figure, we mark red galaxies, classified as described in Section 2.3 as red points, galaxies with $F606W-F814W < 0.6$ as blue points, and intermediate color galaxies as light blue points. The non-red cluster population is divided into two groups in this way to better highlight the locations of the bluest galaxies, in order to understand whether they have discernibly distinct morphologies according to this analysis. RPS galaxies are shown as solid black stars and PSB galaxies as open black squares. We also separate our RPS galaxy sample based on the lengths of the $H\alpha$ tails measured by Moretti et al. (2022). Galaxies with tails longer than 20 kpc are marked with solid black stars, and galaxies with tails shorter than this are marked with open black stars.

For the populations of red and blue galaxies, we show the KDE as correspondingly colored contours. For the PSB galaxies as well as the long- and short-tailed RPS galaxies, we plot the median and standard deviation as error bars, marked with the relevant icon as appropriate. This is done in order to highlight the general distributions of each population in parameter space. We include in the figure the line of $A = 0.35$ from Conselice et al. (2003), which was given as a threshold to select merging galaxies. While we do not classify merging galaxies in this study, it is useful to understand how our sample would be interpreted using this morphological criterion. We note that this threshold is subject to variation, as the measured asymmetry can vary with image resolution and depth (Lotz et al. 2004; Sazonova et al. 2021; Thorp et al. 2021) and the *statmorph* asymmetries are lower than those used in Conselice et al. (2003) (Rodríguez-Gomez et al. 2019), but include the threshold for reference as an indicator of *significant* asymmetry.

The parameters Gini and M_{20} were combined in the top right panel of Figure 8 for both A2744 and A370, with each sample marked and colored as described above. We include in the figure the lines used in Lotz et al. (2008) to separate different types of galaxies in Gini, M_{20} space:

$$\text{mergers: } G > -0.14 M_{20} + 0.33;$$

$$\text{E/S0/Sa: } G \leq -0.14 M_{20} + 0.33 \text{ and } G > 0.14 M_{20} + 0.80;$$

$$\text{Sb - Ir: } G \leq -0.14 M_{20} + 0.33 \text{ and } G \leq 0.14 M_{20} + 0.80;$$

As with the asymmetry threshold, while we do not actively classify these types of galaxies in our sample, we include these lines to compare our sample with the classifications given by these criteria.

We find that the RPS galaxies are spread across a wide range of concentrations, similarly to the rest of the cluster galaxies. The bluest galaxies, with $F606W-F814W < 0.6$, appear to be less concentrated on average compared with the red galaxies. The asymmetry provides a more prominent separation between our disturbed sample and the cluster galaxies, with the PSB galaxies located slightly higher than the average, and the RPS galaxies exhibiting much higher values compared with both the PSB galaxies and the rest of the cluster galaxies. The galaxies with long $H\alpha$ tails in the MUSE data have, on average, higher asymmetries in the broadband data compared with those with shorter $H\alpha$ tails, suggesting that the visual disturbance in broadband imaging is correlated with the underlying ionized

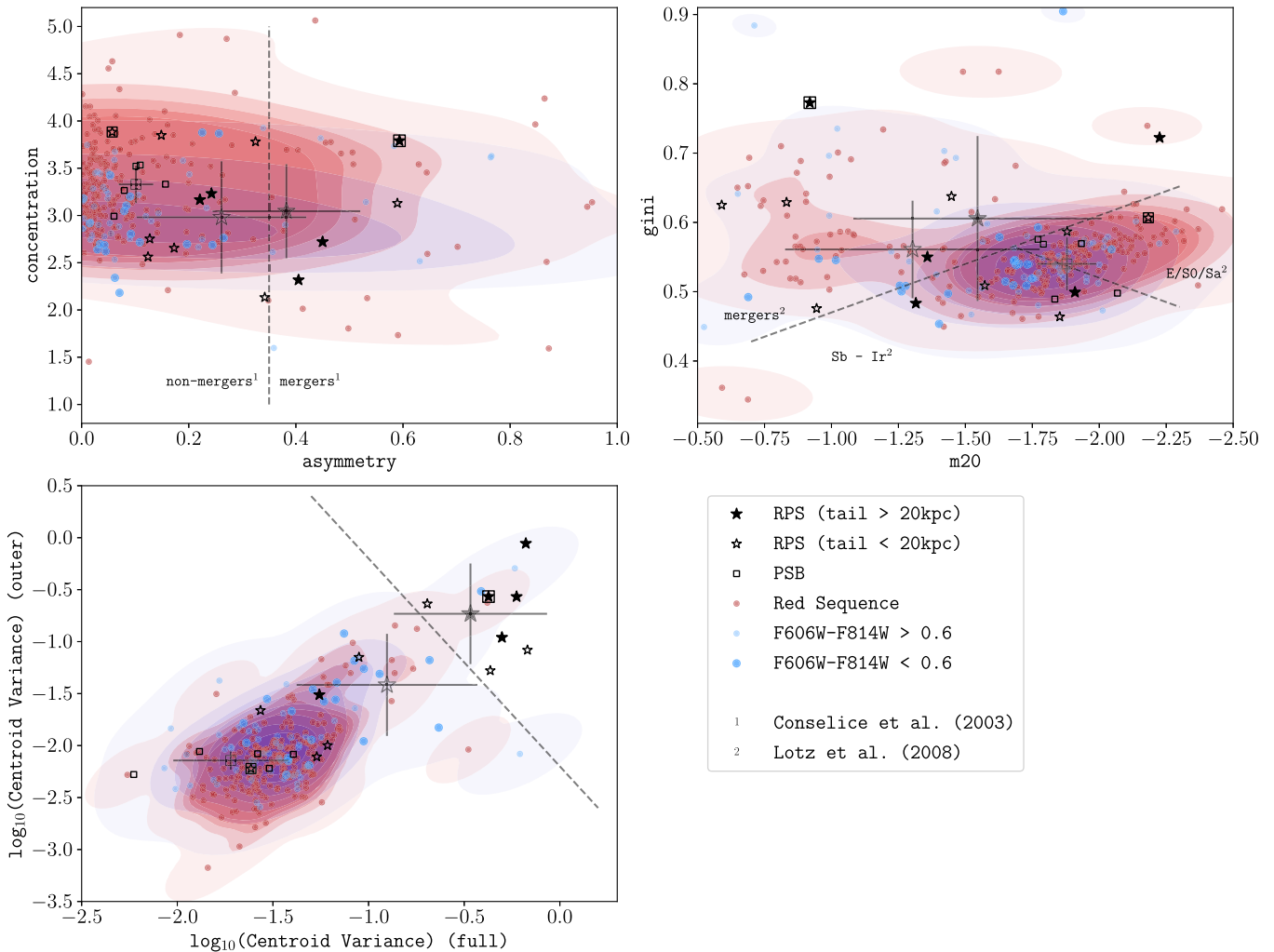


Figure 8. Morphological parameters for galaxies within A2744 and A370 combined. Galaxies are colored accordingly as described in the color–magnitude diagrams, Figure 1. RPS galaxies are marked with solid black stars if they have $H\alpha$ tails longer than 20 kpc according to Moretti et al. (2022) and open black stars otherwise. PSB galaxies are marked with open black squares. A2744_01 (black star in a hollow square) and A2744_07 (hollow star in a hollow square) are thus marked as both RPS and PSB as explained in Section 2.4. *Upper left:* plot of the concentration and asymmetry parameters, derived as described in the text. The median and the standard deviation of concentration and asymmetry within each category are shown as error bars marked with the relevant color or symbol. *Upper right:* plot of the Gini and M_{20} parameters, derived as described in the text. The median and the standard deviation of Gini and M_{20} within each category are shown as error bars marked with the relevant color or symbol. *Lower left:* plot of the outer and full centroid variance parameters, derived as described in the text. The median and the standard deviation of the centroid variance within each category are shown as error bars marked with the relevant color or symbol.

gas disturbance. Comparing the sample with the $A > 0.35$ line, we find that the majority of our long-tailed RPS galaxies would be classified as mergers by this criterion, while most of the short-tailed RPS galaxies and PSB galaxies lie below the threshold. This suggests that while the $A > 0.35$ criterion is useful for selecting disturbed morphologies, it cannot be solely relied upon to distinguish the underlying cause of the disturbance without making considerations about the environment of the galaxies.

The Gini and M_{20} parameters on their own do not strictly separate the RPS or PSB galaxies from the rest of the cluster sample, but when combined, we see that the bulk of the red cluster galaxies are located in a small region as shown in the middle right of the figure, while our sample of PSB galaxies are generally located around the outskirts of this region and the RPS galaxies occupy a much wider range of values, generally being found away from this concentrated region of cluster galaxies. The blue galaxies are fairly scattered in this figure; however, there is a high concentration of galaxies with

$F814W < 0.6$ in the Sb-Ir region. The galaxies with short and long $H\alpha$ tails are not particularly differentiated by their Gini and M_{20} values. We find that the mean values of the long and short-tailed RPS galaxies lie within the merger region given by the Lotz et al. (2008) criteria. As with the asymmetry criterion, this implies that such criteria cannot distinguish between merging and RPS galaxies, and that samples of merging galaxies selected using these criteria may also include galaxies disturbed by ram pressure.

In both the concentration, asymmetry, and the Gini, M_{20} figures, the galaxies A2744_01 and A2744_07 are located in opposite regions of the morphology space. Both of these galaxies exhibit RPS and PSB features (with A2744_01 being primarily RPS and A2744_07 primarily PSB) and are likely to be in an intermediate phase between the two types. Their extreme locations in morphology space therefore suggest that the visual indicators of the disturbance are at their highest toward the end of the RPS phase, and are quick to vanish after the stripping ceases.

5.1. Centroid Variance Method

Each of the above methods provide useful ways to quantify various aspects of the morphologies; however, the disturbed morphologies of the ram-pressure stripped sample do not generally occupy specific regions of any given parameter space, but overlap with the general cluster population.

Here we test methods to detect the low surface-brightness tails and disturbances characteristic of RPS interactions, with the aim of developing a criterion that is tailored to be more sensitive to such objects. To this end, we experiment with measuring the variation between the centroids of flux isocontours to quantify inconsistencies in the light distribution of the galaxy. RPS is often characterized by offset low surface-brightness emission, which will cause the centroids of isocontours taken at different flux levels to vary more than they would in an undisturbed galaxy.

The technique is summarized as follows. We first mask the galaxy with the segmentation map, and take the range of flux values between the minimum and maximum values in the masked image. We ignore the lowest 20% of this range, as the faintest contours tend to be clipped by the segmentation mask and do not reflect the shape of the galaxy's light distribution. We draw a set of eight contours, between 20% and 99% of the flux range, and for comparison an additional set of eight contours focused only on the outer regions of the galaxy between 20% and 50% of the flux range.

For each flux value, we draw an isocontour of the emission, and obtain the position of the non-flux-weighted centroid of that contour using the center-of-mass method from the python package SCIPY. For axisymmetric emission, such as an undisturbed circular or elliptical Gaussian, the centroids of every contour would be expected to lie in exactly the same location. Any disturbances or asymmetries in the light distribution will manifest as variations in the centroid locations.

We then calculate the variance and covariance of the set of coordinates over all of the centroids, normalized by the galaxy's half-light radius, to quantify the movement of the centroids across the different flux thresholds, using the equations:

$$\text{centroid variance} = \frac{\sigma^2(X) + \sigma^2(Y)}{r_e}$$

$$\text{centroid covariance} = \frac{|\text{cov}(X, Y)|}{r_e},$$

where X and Y are the arrays of x and y coordinates of the flux isocontour centroids and r_e is the galaxy half-light radius.

A higher variance indicates that the distribution of flux is nonuniform or asymmetric, while a high covariance indicates that the disturbance is along a particular direction. We found that the variance of the centroid offers a promising indicator of disturbance. The covariance performs similarly well, with slightly less separation between disturbed and undisturbed morphologies.

An example is shown in Figure 9 for A370_08, which shows the contours between 20% and 99% of the range of flux values, and the centroids of each contour as x markers colored accordingly. The skewed light distribution resulting from the disturbance pushes the centroids of the lower surface-brightness emission toward the lower left of the figure relative to the central peak, resulting in an increased variance.

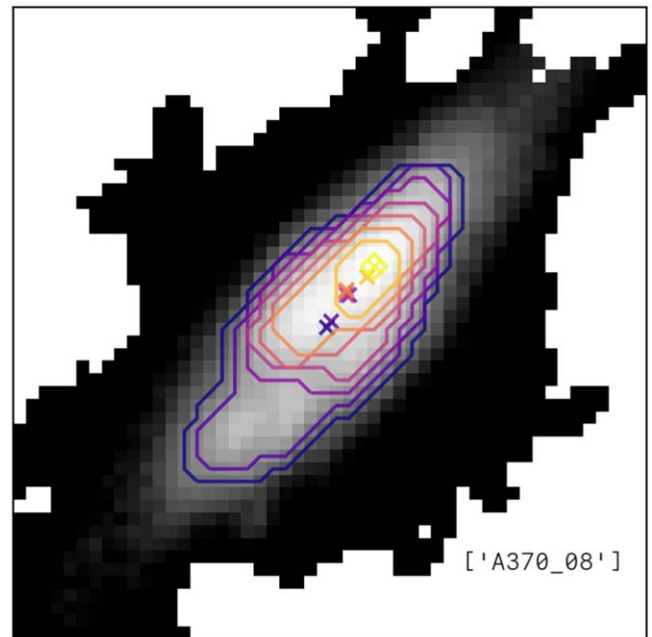


Figure 9. Example of centroid variance measurement on the RPS galaxy A370_08. The F606W image of the galaxy is shown overlaid with the flux isocontours and their corresponding centroids as x markers.

A scatter plot of the centroid variance in the outer region versus the full range is shown in the lower left panel of Figure 8. The figure shows that the majority of galaxies in the RPS sample have significantly higher centroid variances than the rest of the cluster sample, using either range of flux values to define the contour levels. The sample of PSB galaxies do not appear to be distinct from the rest of the cluster galaxies, as is the case for the other morphological parameters. The red cluster galaxies are fairly concentrated with low centroid variances, with the blue galaxies and galaxies with $F606W-F814W < 0.6$ having slightly higher centroid variances in the outer regions in comparison. The distinction between the stripped galaxies and the rest of the cluster sample suggests that the variance in the non-flux-weighted centroid of emission across different flux thresholds is a promising indicator of disturbed morphologies and could feasibly be used to detect galaxies of interest. It is possible that disturbances due to non-RPS processes, e.g., tidal interaction, could affect the centroids in a similar way; however, on inspection of the non-RPS objects that are close to our RPS sample in the figure, we do not see evidence of gravitational disturbances, and a dedicated sample would be required to test the classification of gravitationally interacting galaxies using this method. A plot of the covariances can be found in Figure 16 in the Appendix, for reference.

To test the success of the centroid variance parameters at resolving the RPS galaxies from the cluster populations, we carried out two sample K-S tests for each morphological parameter.

We found that at the 5% significance level, the *concentration* ($p = 0.12$) and *Gini* ($p = 0.16$) parameters cannot distinguish the RPS galaxies from the distribution of undisturbed cluster galaxies, whereas for the *asymmetry* ($p = 2.84 \times 10^{-5}$), M_{20} ($p = 0.04$), outer centroid variance ($p = 4.13 \times 10^{-6}$), and full centroid variance ($p = 7.11 \times 10^{-7}$) parameters, the RPS galaxies are distinct from the undisturbed cluster population.

Table 1

Table of Weights ω_i Assigned to Each of the Input Variables x_i to Yield the Principal Components in the Linear Combination $\omega_1x_1 + \omega_2x_2 + \omega_3x_3 + \dots$

Input Variable x_i	Weights ω_i		
	PC1	PC2	PC3
Concentration	-0.276	-0.073	0.481
Asymmetry	0.160	0.654	-0.126
Gini	-0.004	0.589	0.387
M_{20}	0.282	0.370	-0.302
$\text{Log}_{10}(\text{centroid var.})$ (outer)	0.474	-0.119	-0.039
$\text{Log}_{10}(\text{centroid covar.})$ (outer)	0.436	-0.113	-0.011
$\text{Log}_{10}(\text{centroid var.})$ (full)	0.457	-0.096	0.324
$\text{Log}_{10}(\text{centroid covar.})$ (full)	0.315	-0.038	0.593
F606W-F814W color	-0.309	0.211	0.234

To test the selection of RPS galaxies using this diagnostic, we draw a line approximately separating the distinct clump of galaxies in the top right from the rest of the sample, described by the equation

$$\log_{10}(\text{outer CV}) > -2 \times \log_{10}(\text{full CV}) - 2.2$$

where outer CV and full CV refer to the outer centroid variance and full centroid variance, respectively. This criterion yields a sample of 10 galaxies, of which four are long-tailed RPS galaxies, three are short-tailed RPS galaxies, and three are non-RPS cluster galaxies.

We calculated the precision and recall of this selection criterion, defined as

$$\text{precision} = \frac{\text{true positives}}{\text{true positives} + \text{false positives}}$$

$$\text{recall} = \frac{\text{true positives}}{\text{true positives} + \text{false negatives}},$$

finding a precision of 0.70 and a recall of 0.58.

5.2. Principal Component Analysis

We applied principal component analysis (PCA) in order to visualize the distribution of these galaxies and investigate whether similar galaxies are grouped together in the combined morphology space. PCA reduces multidimensional parameter space by finding the *principal components* of covariant parameters, in order to explore relations between different parameters, or simplify the visualization of a large number of parameters that may all scale according to some common underlying property. In this case, each of the morphological parameters gives us complementary, but overlapping information about the shape of a galaxy. By normalizing each of the different quantities to negate the effects of scale, and transforming them into a reduced parameter space, we can retain the maximum amount of information with a simplified set of quantities. PCA transforms data into a set of orthogonal eigenvectors, or principal components, which are linear combinations of the input parameters. These are arranged such that the maximum amount of variance from the original data is contained in the first few eigenvectors of the transformed data set.

To select the number of relevant principal components, we use the rule proposed by Kaiser (1960), whereby components are rejected if they contain less than the expected variance of uncorrelated variables. In this case, with nine variables at play,

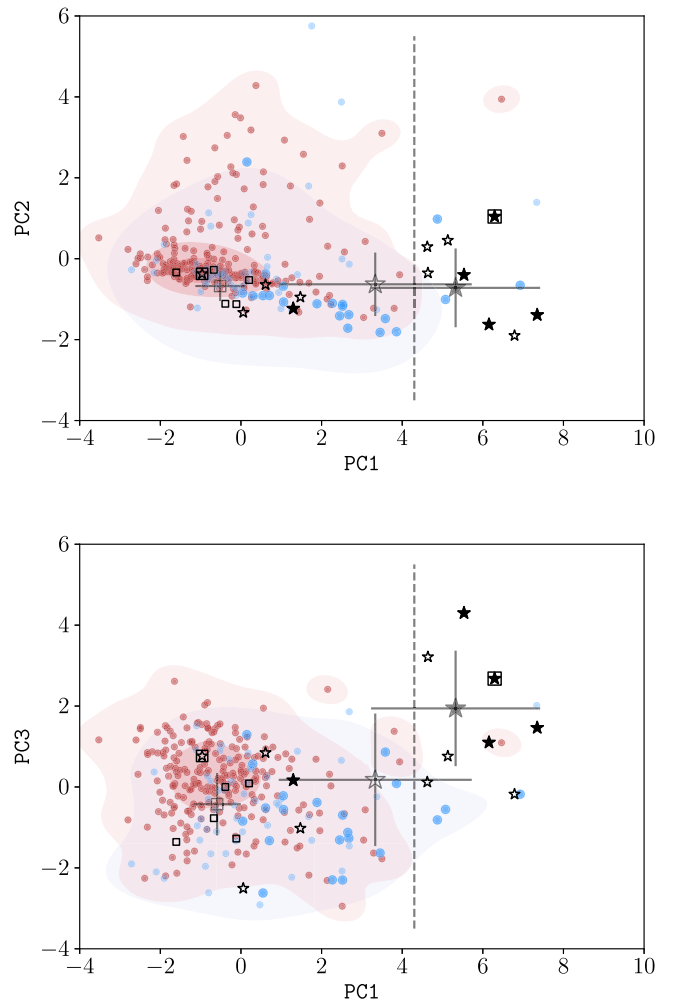


Figure 10. Scatter plots of the three components resulting from the PCA described in the text, for all cluster members in A2744 and A370 combined. Data points are colored or indicated by symbols as described in Figure 8. The median and the standard deviation of the two components within each category are shown as error bars marked with the relevant color or symbol. The vertical dashed line indicates the $\text{PC1} > 4.3$ threshold suggested here to select potential ram-pressure-stripped galaxies.

each would contain 11.1% of the total sample variance if no correlation was present. We find that three principal components are above this threshold, which altogether contains 67% of the total sample variance (PC1: 37%, PC2: 16%, PC3: 13%). Notably, the first principal component contains more than double the sample variance of each of the other components. The variances of the top five principal components yielded by the PCA are shown graphically in Figure 14 in the Appendix.

The principal components resulting from the PCA are described in Table 1. The input parameters (each of the morphological quantities) are given in the first column of the table. To obtain each of the principal components PC1, PC2, and PC3 of Table 1, respectively) are scaled by their corresponding weights (given in columns PC1, PC2, and PC3 of Table 1, respectively) and combined in summation (i.e., $\text{PC1} = -0.276 \times \text{concentration} + 0.16 \times \text{asymmetry} - 0.004 \times \text{Gini} + \dots$). The first principal component, PC1, which contains significantly more of the sample variance than the other components, is most influenced by the outer centroid variance and full centroid variance parameters, with weights of 0.474 and 0.457, respectively. PC2 is driven mostly by asymmetry and

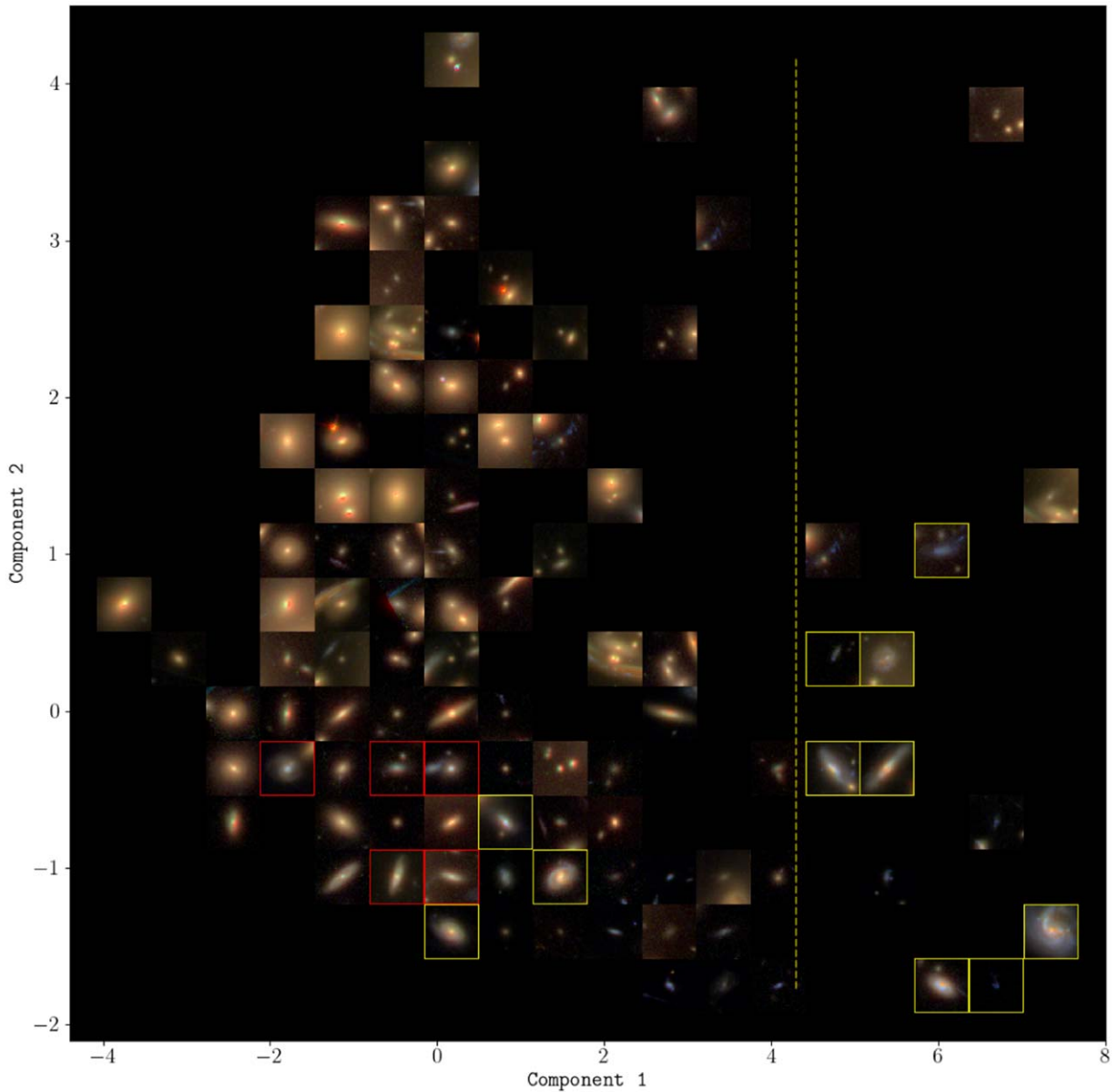


Figure 11. Grid of sample galaxies in the dimensionally reduced space yielded by the PCA described in Section 5. At each location on the grid, an example galaxy is shown in order to visualize the different morphologies that occupy different regions of the reduced morphology space. RPS and PSB galaxies are marked with yellow and red borders, respectively. If multiple types occupy a bin, priority is given to showing RPS galaxies, then PSB galaxies, then undisturbed cluster galaxies. The yellow dashed line indicates the $PC1 > 4.3$ threshold described in the text, above which the majority of RPS galaxies are found.

Gini, while $PC3$ is influenced mostly by the full centroid covariance and the concentration. All of the components, however, are non-negligibly influenced by several other parameters in addition to these.

The sample of galaxies is displayed reprojected into the resulting principal component space in Figure 10. These three components on their own do not describe physical properties, but help to visualize any groupings of galaxies in higher dimensional parameter space in a simplified plot.

The three components are shown in Figure 10, with $PC1$ compared with $PC2$ in the upper panel, and with $PC3$ in the lower panel.

It is clear from the figure that $PC1$ provides the strongest separation between the RPS sample and the cluster galaxies, with the vertical line at $PC1 = 4.3$ drawn on the figure to mark our suggested threshold.

This criterion of $PC1 > 4.3$ selects 4/5 long-tailed RPS galaxies, 4/7 short-tailed RPS galaxies, as well as four blue galaxies and one red galaxy. We calculated a precision of 0.62 and a recall of 0.67 for the threshold of 4.3, and additionally show the two diagnostics calculated over a range of threshold values shown in Figure 15 in the Appendix. In comparison, the precision of this selection is slightly lower than when selecting galaxies using only the centroid variance measurements, but the recall is higher, i.e., the PCA selection retrieved more of the known RPS sample.

We further inspected the non-RPS sample objects and found that two of the blue objects in this region of the diagram are clumps that are close in location and velocity to A2744_01 and A370_08, strongly suggesting that they are clumps of material associated with those galaxies, which have been flagged as distinct objects by the source extraction but indeed are

considered part of the jellyfish tail by our MUSE analysis (Moretti et al. 2022). The latter of those two objects, the clump to the south of A370_08, is likely to be the object identified as CL49 in Lagattuta et al. (2017, 2019), which the authors also concluded was a clump of material detached from the main galaxy. Two sources, the red object and one of the blue objects, were found to be galaxies overlapping in projection. The last blue object was inspected and found to have associated emission lines in the MUSE image, however, the object is very small and faint, and while it appears to be disturbed in the HST image, the nature of the disturbance cannot be verified.

The distribution of galaxies across PC1 and PC2 is also shown in Figure 11, with the space divided into bins and an example galaxy shown for each bin to indicate typical morphologies corresponding to that combination of parameters. In general, the lower left corner of the figure appears to contain the majority of undisturbed spiral galaxies as well as elliptical and spheroidal galaxies. Moving upward toward the top-left companions that may be impacting their morphological parameters. Moving toward the bottom right, the galaxies appear to have increasingly disturbed morphologies, which is where most of our RPS sample is located.

6. Discussion and Summary

We have analyzed a sample of 12 RPS galaxies and six PSB galaxies within two clusters at intermediate redshift, A2744 and A370. We have compared several characteristics of the RPS and PSB galaxies with the general cluster population, specifically, their orbital information, their distribution within cluster substructures and environment, and their morphologies.

We found that the general cluster population in the observed field of A2744 follows a bimodal distribution, with the two components having similar velocities to the regions described as the SMRC and the NC in Owers et al. (2011). All of the RPS galaxies, and all but one of the PSB galaxies are located in the blueshifted structure, along with a significantly higher fraction of blue galaxies in comparison with the redshifted component. Together, this is indicative that the collision of the galaxies in the CTD with the X-ray gas associated with the SMRC is responsible for the stripping being experienced by the RPS galaxies. The difference in blue fractions between the substructures may be due to an excess of blue galaxies in the blueshifted component caused by increased star formation due to weak stripping, or a dearth of blue galaxies in the redshifted component resulting from quenching during a previous merger event.

We find that in A370, the RPS galaxies and PSB galaxies are more evenly distributed in phase space and the majority are not residing in any substructures. While A370 is also a merging cluster, we do not see any evidence that the observed RPS galaxies are the result of the merger, instead they are more likely to be isolated infalling galaxies.

We analyzed the ICM X-ray emission at the locations of the cluster galaxies, and found that in both clusters the PSB galaxies reside in regions of higher ICM X-ray flux compared with the blue cluster members and RPS galaxies. In A370 the RPS galaxies are also located at higher ICM X-ray fluxes than

the blue cluster galaxies, but not as high as the PSB galaxies. The location of the PSB galaxies in regions of higher ICM X-ray flux, which scales with gas density, is consistent with the population of PSB galaxies being produced, at least in part, by ram-pressure interactions.

Finally, we implemented several measures to quantify the morphologies of the galaxies and compared the results for the different samples. We utilized concentration, asymmetry, Gini, and M_{20} , and also tested whether the variance and covariance of the emission centroid of different flux isocontours could be a useful measure of the disturbance caused by RPS.

We found that the most effective standalone measure of the morphology was the centroid variance, which shows promise as a potential measure to detect disturbed morphologies. By combining the different parameters using PCA, the scatter was further reduced and the separation of both weakly and strongly disturbed galaxies from the general cluster population was made clearer than when using any of the individual morphological quantities alone. This could have practical applications for filtering through large broadband imaging data sets for potentially disturbed galaxies prior to manual inspection to determine the cause of the disturbance, reducing the workload on human classifiers. These kinds of automated techniques will open up the possibility of detecting samples of RPS candidates from huge catalogs of survey data, including, as we have found, cases where the disturbance is minimal in the broadband images. By expanding the known RPS samples and obtaining snapshots of galaxies from first infall to fully quenched, we will be able to further explore the process of RPS and its impact on galaxies in clusters.

We wish to thank D. J. Lagattuta for valued comments and suggestions. We are grateful to the anonymous referee who helped us clarify and strengthen this analysis. This project has received funding from the European Research Council (ERC) under the European Unions Horizon 2020 research and innovation program (grant agreement No. 833824, GASP project). We acknowledge funding from the INAF main-stream funding program (PI: B. Vulcani) and the Italian PRIN-Miur 2017 (PI: A. Cimatti). Y.J. gratefully acknowledges support from the ANID BASAL project FB210003.

Software: Astropy (Astropy Collaboration et al. 2013, 2018), statmorph (Rodriguez-Gomez et al. 2019), SINOPSIS (Fritz et al. 2017), HIGHELF.

Appendix Additional Figures

We include here several additional figures for reference. See Figures 12 and 13 for overviews of the clusters A2744 and A370, respectively. Figure 14 shows the variance of the principal components yielded by the PCA, whilst Figure 15 shows the values of precision and recall for different selection thresholds of PC1. Figure 16 shows the outer and full centroid variance parameters, calculated in the morphology analysis. Figure 17 shows segmentation maps and morphology diagnostics for several examples.

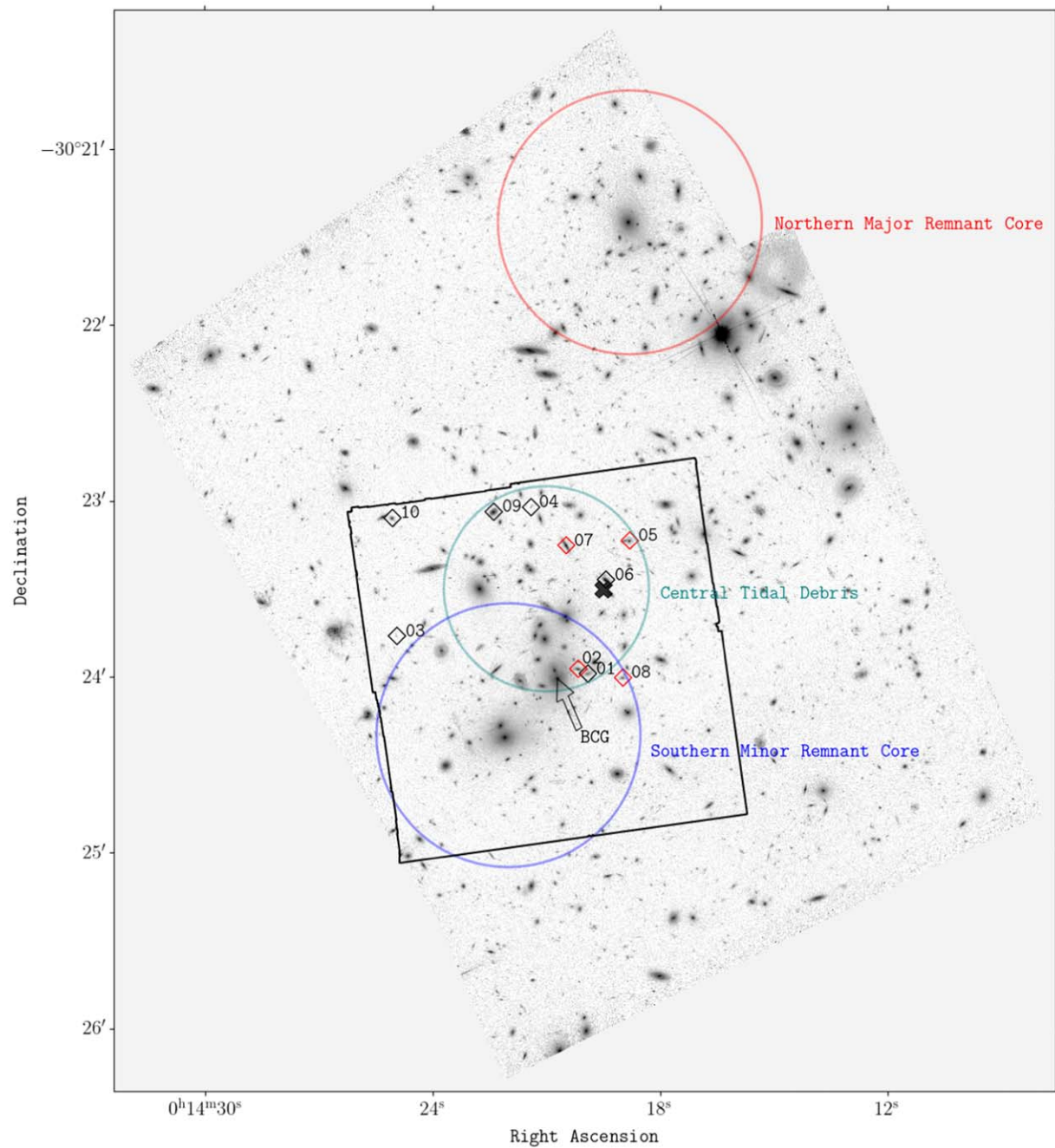


Figure 12. Overview of A2744 showing the HST F606W image of the cluster, with the MUSE footprint shown by the black square. Locations of the different cluster regions as defined in Owers et al. (2011) are overlaid as colored circles, the RPS and PSB galaxies are shown by the black and red diamonds, respectively. The arrow marks the BCG used as the center for this analysis and the black X marks the X-ray surface-brightness peak measured by Owers et al. (2011).

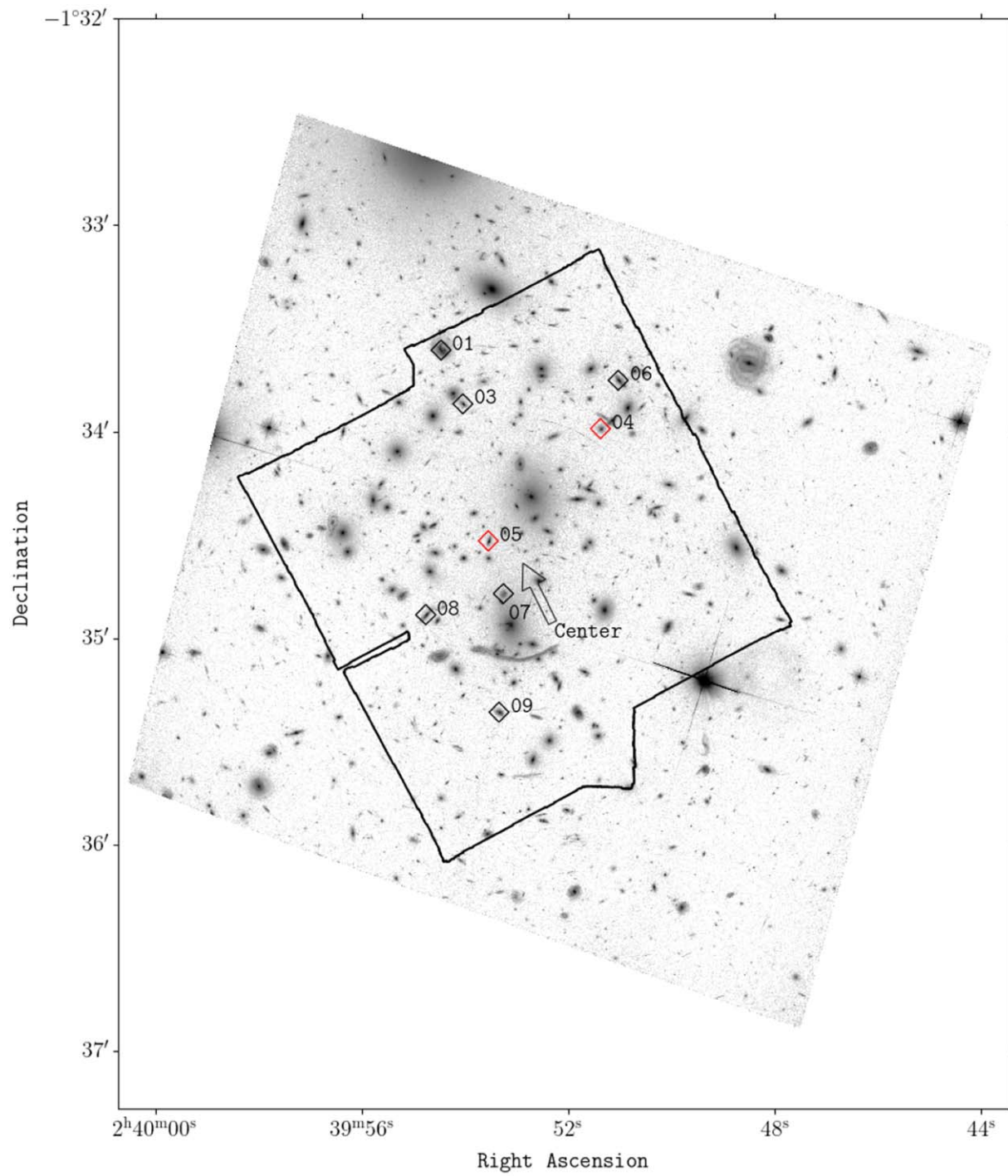


Figure 13. Overview of A370 showing the HST F606W image of the cluster, with the MUSE footprint shown by the black square. RPS and PSB galaxies are shown by the black and red diamonds, respectively. The arrow marks the point between the two BCGs used as the center for this analysis.

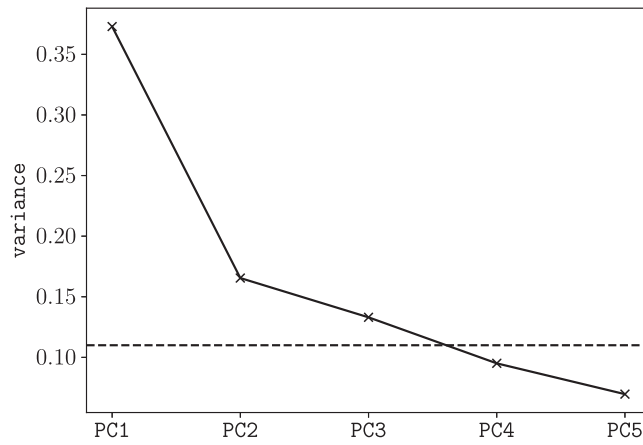


Figure 14. Variance of the top five principal components yielded by the PCA. The horizontal dashed line shows the cutoff of 11.1%, below which a principal component was not used, as described in Section 5.2.

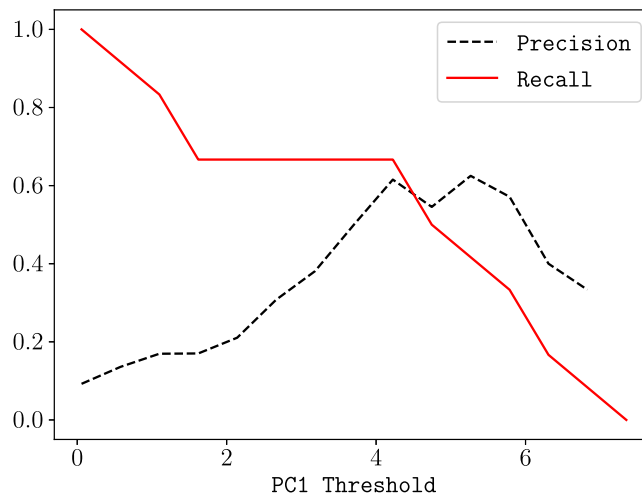


Figure 15. Values of precision and recall calculated across the range of selection thresholds for PC1. The selected value of 4.3, chosen in the analysis, is close to the crossover between the two diagnostics as well as the peak in the precision.

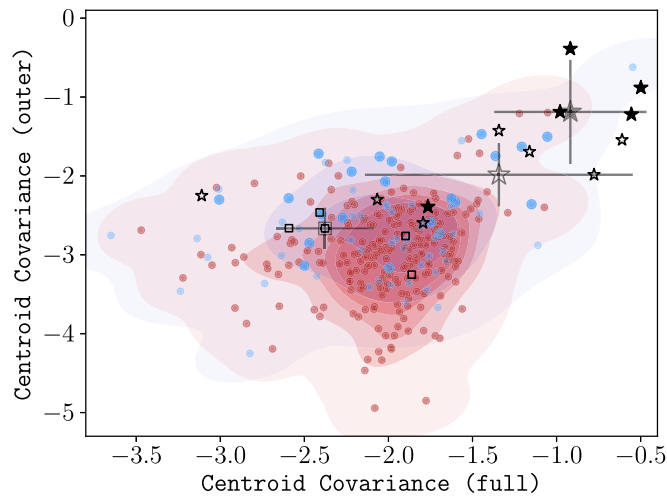


Figure 16. Plot of the outer and full centroid covariance parameters for galaxies within A2744 and A370 combined, derived as described in the text. The median and the standard deviation of the centroid covariance within each category are shown as error bars marked with the relevant color or symbol. Galaxies are colored accordingly as described in the color–magnitude diagrams, Figure 1, and marked as described in Figure 8.

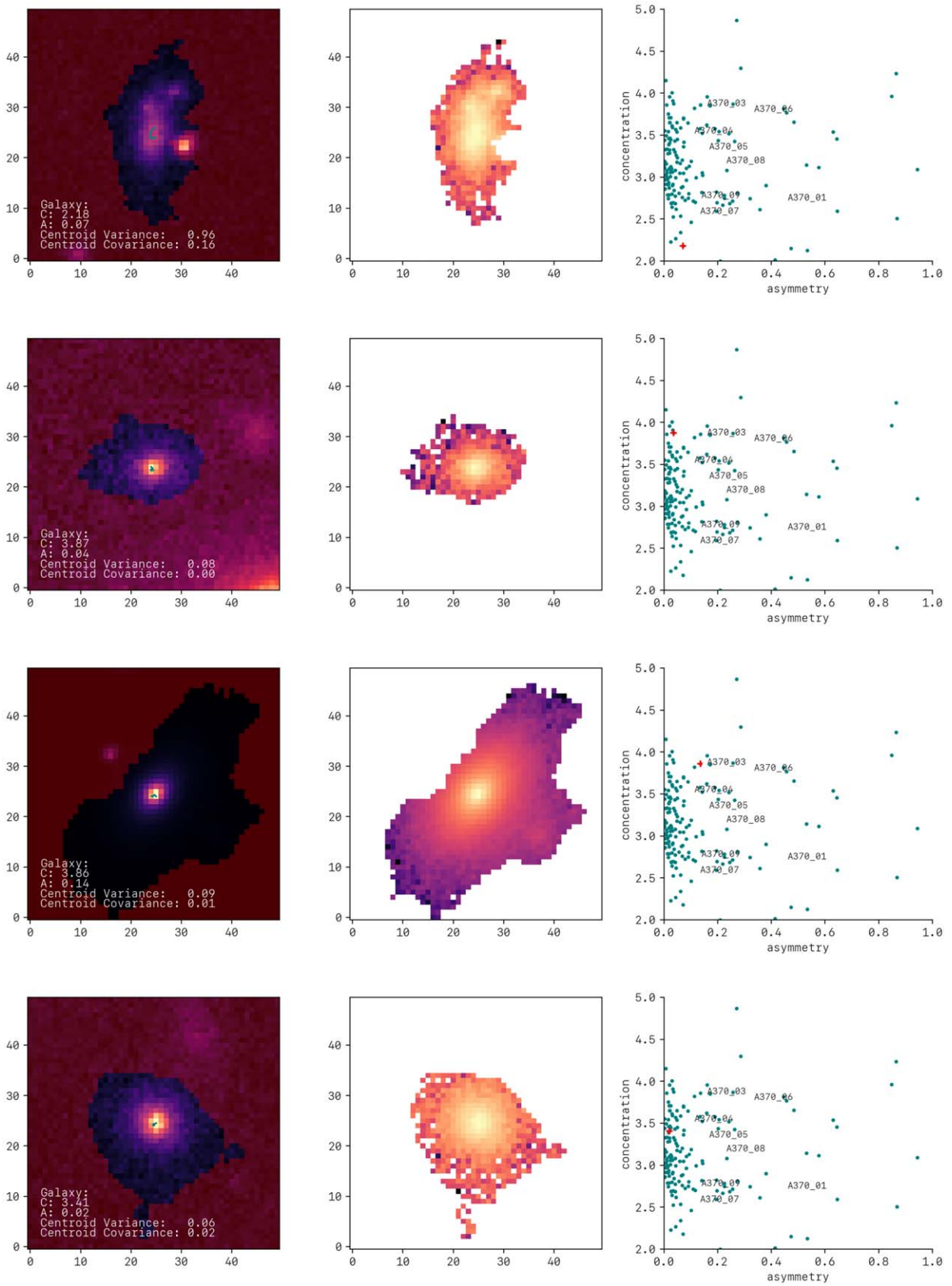
















Figure 17. Example morphology diagnostics and segmentation maps, showing some cases where a galaxy has a close neighbor and some deblending has been required to produce the segmentation map.

ORCID iDs

Callum Bellhouse  <https://orcid.org/0000-0002-6179-8007>
 Bianca Poggianti  <https://orcid.org/0000-0001-8751-8360>
 Alessia Moretti  <https://orcid.org/0000-0002-1688-482X>
 Benedetta Vulcani  <https://orcid.org/0000-0003-0980-1499>
 Ariel Werle  <https://orcid.org/0000-0002-4382-8081>
 Marco Gullieuszik  <https://orcid.org/0000-0002-7296-9780>
 Mario Radovich  <https://orcid.org/0000-0002-3585-866X>
 Yara Jaffé  <https://orcid.org/0000-0003-2150-1130>
 Jacopo Fritz  <https://orcid.org/0000-0002-7042-1965>
 Alessandro Igesti  <https://orcid.org/0000-0003-1581-0092>
 Cecilia Bacchini  <https://orcid.org/0000-0002-8372-3428>
 Neven Tomičić  <https://orcid.org/0000-0002-8238-9210>
 Johan Richard  <https://orcid.org/0000-0001-5492-1049>
 Geneviève Soucail  <https://orcid.org/0000-0001-9976-1237>

References

- Abraham, R. G., van den Bergh, S., & Nair, P. 2003, *ApJ*, 588, 218
 Astropy Collaboration, Price-Whelan, A. M., Sipőcz, B. M., et al. 2018, *AJ*, 156, 123
 Astropy Collaboration, Robitaille, T. P., Tollerud, E. J., et al. 2013, *A&A*, 558, A33
 Bacon, R., Accardo, M., Adjali, L., et al. 2010, *Proc. SPIE*, 7735, 773508
 Bacon, R., Conseil, S., Mary, D., et al. 2017, *A&A*, 608, A1
 Balogh, M. L., Navarro, J. F., & Morris, S. L. 2000, *ApJ*, 540, 113
 Beers, T. C., Flynn, K., & Gebhardt, K. 1990, *AJ*, 100, 32
 Bellhouse, C., McGee, S. L., Smith, R., et al. 2021, *MNRAS*, 500, 1285
 Boschin, W., Girardi, M., Spolaor, M., & Barrena, R. 2006, *A&A*, 449, 461
 Boselli, A., Epinat, B., Contini, T., et al. 2019, *A&A*, 631, A114
 Boselli, A., & Gavazzi, G. 2006, *PASP*, 118, 517
 Butcher, H., & Oemler Jr., A. 1978a, *ApJ*, 219, 18
 Butcher, H., & Oemler Jr., A. 1978b, *ApJ*, 226, 559
 Butcher, H., & Oemler Jr., A. 1984, *ApJ*, 285, 426
 Conselice, C. J. 2003, *ApJS*, 147, 1
 Conselice, C. J. 2014, *ARA&A*, 52, 291
 Conselice, C. J., Bershad, M. A., Dickinson, M., & Papovich, C. 2003, *AJ*, 126, 1183
 Dressler, A. 1980, *ApJ*, 236, 351
 Dressler, A., Oemler, A. J., Couch, W. J., et al. 1997, *ApJ*, 490, 577
 Dressler, A., & Shectman, S. A. 1988, *AJ*, 95, 985
 Dressler, A., Smail, I., Poggianti, B. M., et al. 1999, *ApJS*, 122, 51
 Durret, F., Chiche, S., Lobo, C., & Jauzac, M. 2021, *A&A*, 648, A63
 Ebeling, H., Edge, A. C., & Henry, J. P. 2001, *ApJ*, 553, 668
 Ebeling, H., & Kalita, B. S. 2019, *ApJ*, 882, 127
 Ebeling, H., Stephenson, L. N., & Edge, A. C. 2014, *ApJL*, 781, L40
 Fossati, M., Fumagalli, M., Boselli, A., et al. 2016, *MNRAS*, 455, 2028
 Fritz, J., Moretti, A., Gullieuszik, M., et al. 2017, *ApJ*, 848, 132
 Fumagalli, M., Fossati, M., Hau, G. K. T., et al. 2014, *MNRAS*, 445, 4335
 Girardi, L., Bressan, A., Chiosi, C., Bertelli, G., & Nasi, E. 1996, *A&AS*, 117, 113
 Glasser, G. J. 1962, *JASA*, 57, 648
 Gullieuszik, M., Poggianti, B. M., Moretti, A., et al. 2017, *ApJ*, 846, 27
 Gunn, J. E., & Gott, J. R., III 1972, *ApJ*, 176, 1
 Hernández-Fernández, J. D., Haines, C. P., Diaferio, A., et al. 2014, *MNRAS*, 438, 2186
 Jaffé, Y. L., Smith, R., Candlish, G. N., et al. 2015, *MNRAS*, 448, 1715
 Jaffé, Y. L., Poggianti, B. M., Moretti, A., et al. 2018, *MNRAS*, 476, 4753
 Jauzac, M., Jullo, E., Eckert, D., et al. 2015a, *MNRAS*, 446, 4132
 Jauzac, M., Richard, J., Jullo, E., et al. 2015b, *MNRAS*, 452, 1437
 Jullo, E., & Kneib, J. P. 2009, *MNRAS*, 395, 1319
 Kaiser, H. F. 1960, *Educ. Psychol. Meas.*, 20, 141
 Kalita, B. S., & Ebeling, H. 2019, *ApJ*, 887, 158
 Kauffmann, G. 1995, *MNRAS*, 274, 153
 Kenney, J. D. P., Geha, M., Jáchym, P., et al. 2014, *ApJ*, 780, 119
 Kneib, A., & Müller, V. 2000, *A&A*, 354, 761
 Lagattuta, D. J., Richard, J., Bauer, F. E., et al. 2019, *MNRAS*, 485, 3738
 Lagattuta, D. J., Richard, J., Clément, B., et al. 2017, *MNRAS*, 469, 3946
 Lah, P., Pracy, M. B., Chengalur, J. N., et al. 2009, *MNRAS*, 399, 1447
 Larson, R. B., Tinsley, B. M., & Caldwell, C. N. 1980, *ApJ*, 237, 692
 Limousin, M., Richard, J., Jullo, E., et al. 2016, *A&A*, 588, A99
 Lotz, J. M., Davis, M., Faber, S. M., et al. 2008, *ApJ*, 672, 177
 Lotz, J. M., Koekemoer, A., Coe, D., et al. 2017, *ApJ*, 837, 97
 Lotz, J. M., Primack, J., & Madau, P. 2004, *AJ*, 128, 163
 Lynds, R., & Petrosian, V. 1986, *BAAS*, 18, 1014
 Mahler, G., Richard, J., Clément, B., et al. 2018, *MNRAS*, 473, 663
 Mantz, A., Allen, S. W., Ebeling, H., Rapetti, D., & Drica-Wagner, A. 2010, *MNRAS*, 406, 1773
 McPartland, C., Ebeling, H., Roediger, E., & Blumenthal, K. 2016, *MNRAS*, 455, 2994
 Merluzzi, P., Busarello, G., Dopita, M. A., et al. 2013, *MNRAS*, 429, 1747
 Merritt, D. 1983, *ApJ*, 264, 24
 Mihos, J. C., & Hernquist, L. 1994, *ApJL*, 425, L13
 Miller, N. A., Oegerle, W. R., & Hill, J. M. 2006, *AJ*, 131, 2426
 Molnar, S. M., Ueda, S., & Umetsu, K. 2020, *ApJ*, 900, 151
 Moore, B., Katz, N., Lake, G., Dressler, A., & Oemler, A. 1996, *Natur*, 379, 613
 Moore, B., Lake, G., & Katz, N. 1998, *ApJ*, 495, 139
 Moretti, A., Radovich, M., Poggianti, B. M., et al. 2022, *ApJ*, 925, 4
 Olave-Rojas, D., Cerulo, P., Demarco, R., et al. 2018, *MNRAS*, 479, 2328
 Owers, M. S., Couch, W. J., Nulsen, P. E. J., & Randall, S. W. 2012, *ApJL*, 750, L23
 Owers, M. S., Randall, S. W., Nulsen, P. E. J., et al. 2011, *ApJ*, 728, 27
 Pawlik, M. M., Wild, V., Walcher, C. J., et al. 2016, *MNRAS*, 456, 3032
 Poggianti, B. M., Bridges, T. J., Komiyama, Y., et al. 2004, *ApJ*, 601, 197
 Poggianti, B. M., Fasnano, G., Omizzolo, A., et al. 2016, *AJ*, 151, 78
 Poggianti, B. M., Jaffé, Y. L., Moretti, A., et al. 2017b, *Natur*, 548, 304
 Poggianti, B. M., Moretti, A., Gullieuszik, M., et al. 2017a, *ApJ*, 844, 48
 Postman, M., Coe, D., Benítez, N., et al. 2012, *ApJS*, 199, 25
 Richard, J., Claeysens, A., Lagattuta, D., et al. 2021, *A&A*, 646, A83
 Richard, J., Jauzac, M., Limousin, M., et al. 2014, *MNRAS*, 444, 268
 Richard, J., Kneib, J. P., Limousin, M., Edge, A., & Jullo, E. 2010, *MNRAS*, 402, L44
 Roberts, I. D., & Parker, L. C. 2020, *MNRAS*, 495, 554
 Rodriguez-Gomez, V., Snyder, G. F., Lotz, J. M., et al. 2019, *MNRAS*, 483, 4140
 Sazonova, E., Alatalo, K., Rowlands, K., et al. 2021, *ApJ*, 919, 134
 Smith, R., Fellhauer, M., & Assmann, P. 2012, *MNRAS*, 420, 1990
 Soucail, G. 1987, *Msngr*, 48, 43
 Soucail, G., Mellier, Y., Fort, B., Mathez, G., & Cailloux, M. 1988, *A&A*, 191, L19
 Spitzer, L. J., & Baade, W. 1951, *ApJ*, 113, 413
 Springel, V. 2000, *MNRAS*, 312, 859
 Stroe, A., Hussaini, M., Husemann, B., Sobral, D., & Tremblay, G. 2020, *ApJL*, 905, L22
 Stroe, A., Sobral, D., Paulino-Afonso, A., et al. 2017, *MNRAS*, 465, 2916
 Thorp, M. D., Bluck, A. F. L., Ellison, S. L., et al. 2021, *MNRAS*, 507, 886
 Toomre, A. 1977, in *Evolution of Galaxies and Stellar Populations*, ed. B. M. Tinsley, R. B. G. Larson, & D. Campbell (New Haven, CT: Yale Univ. Observatory), 401
 Tinsley, B. M., & Larson, R. B. 1979, *MNRAS*, 186, 503
 Treu, T., Schmidt, K. B., Brammer, G. B., et al. 2015, *ApJ*, 812, 114
 Umetsu, K., Broadhurst, T., Zitrin, A., et al. 2011a, *ApJ*, 738, 41
 Umetsu, K., Broadhurst, T., Zitrin, A., Medezinski, E., & Hsu, L.-Y. 2011b, *ApJ*, 729, 127
 Vijayaraghavan, R., & Ricker, P. M. 2013, *MNRAS*, 435, 2713
 Vollmer, B., Cayatte, V., Balkowski, C., & Duschl, W. J. 2001, *ApJ*, 561, 708
 von der Linden, A., Allen, M. T., Applegate, D. E., et al. 2014, *MNRAS*, 439, 2
 Vulcani, B., Poggianti, B. M., Smith, R., et al. 2022, *ApJ*, 927, 91
 Vulcani, B., Treu, T., Nipoti, C., et al. 2017, *ApJ*, 837, 126
 Vulcani, B., Poggianti, B. M., Gullieuszik, M., et al. 2018, *ApJL*, 866, L25
 Vulcani, B., Treu, T., Schmidt, K. B., et al. 2016, *ApJ*, 833, 178
 Werle, A., Poggianti, B., Moretti, A., et al. 2022, *ApJ*, 930, 43